Surfactant Adsorption and Marangoni Flow in Liquid Jets. 2. Modeling

Michael Weiss and Richard C. Darton*

Department of Engineering Science, University of Oxford, Parks Road, Oxford OX1 3PJ, United Kingdom

Turgut Battal† and Colin D. Bain

Physical and Theoretical Chemistry Laboratory, University of Oxford, South Parks Road, Oxford OX1 3QZ, United Kingdom

This paper is concerned with the interfacial behavior of surfactant solutions on short time scales. A gravity-driven laminar liquid jet is used to create a rapidly expanding liquid surface, which exposes the surfactant solution to highly nonequilibrium conditions. This expansion causes the surface tension to differ locally from its equilibrium value, generating a (Marangoni) shear stress that acts on the jet surface and retards the surface acceleration. A theory for the flow very near the nozzle shows that the cube-root dependence of the surface velocity on the distance traveled is altered through the adsorption of surfactant. In a boundary-layer treatment, both the surface velocity and the surface concentration increase linearly from the nozzle exit over a short distance, which we term the detachment region. The length of the detachment region is found to vary with the bulk concentration raised to the power $^3/_2$. A numerical model of the surfactant adsorption process in the jet has been developed within the framework of the CFD code FIDAP. The numerical solution confirms the general features of the theory and shows that the maximum reduction in surface velocity occurs very close to the nozzle exit, except at high concentrations. A comparison with experiments on C_{16}TAB at concentrations below the critical micelle concentration, which are described in part 1 of this series of papers, shows good agreement.

1. Introduction

The study of the behavior of surfactant solutions away from equilibrium is of considerable interest. One example found in nature is our ability to breathe, which is facilitated by surfactants in the lung.[1] Examples found in industry include emulsification, multiphase flow, detergency, wetting, coating, and foaming.[2−4] During drainage in a foam, film thinning occurs. In the thin part of the film, the surface concentration of the surface-active solute falls with a resulting rise in the local surface tension. Consequently, a surface force acts toward the region of high surface tension. This force causes a counter surface flow of liquid that opposes film drainage and restores the film.[5]

This paper is concerned with the study of the dynamics of surfactant adsorption at a continually expanding surface on short time scales (<1−100 ms). A gravity-driven, vertical, laminar liquid jet is employed to create such an expanding surface. The investigation is carried out experimentally, using noninvasive optical techniques—laser Doppler velocimetry and ellipsometry—to measure the fluid mechanics and the amount of surfactant adsorbed at the surface. The experimental work has been described in part 1 of this series of papers.[6] A mathematical model has been developed within the framework of the commercial CFD code FIDAP, which simulates the adsorption process in the jet. This modeling work is described here.

The liquid jet used in this study issues from a long circular capillary pipe. The inner diameter of the pipe is on the order of 1 mm, and its length was chosen to be 100 times the nozzle diameter, sufficiently long to ensure fully developed laminar flow at the nozzle exit. The long pipe is attached to a liquid reservoir in which the liquid height is maintained at a constant level. Gravity provides the driving force for the liquid flow. The liquid leaves the nozzle with a mean velocity that is on the order of 1 m s^{-1}. The nozzle end is tapered to minimize wetting at the tip of the nozzle. The contraction of the jet is only slight, which is due to the high Reynolds number.

Before giving an account of our CFD model of the jet flow, we model the jet flow analytically in the absence and in the presence of surfactant, within a boundary-layer formalism. Using continuity and conservation of axial momentum, we derive the well-established cube-root dependence of surface velocity and jet contraction on the axial distance. We then show how this characteristic behavior changes in the presence of surfactant. The surface velocity then varies linearly with distance near to the nozzle, as a result of a limiting Marangoni stress at that point, and the surface expansion rate at the point of detachment from the nozzle remains finite. The singular behavior of the jet flow at the nozzle exit is thus eliminated. This limitation of the Marangoni stress at the nozzle exit is implemented in the numerical model.

Next, a complete fluid mechanic model of the jet for a pure liquid (water) is introduced. The governing equations and the boundary conditions are given,

* To whom correspondence should be addressed. Tel.: +44 1865 273117. Fax: +44 1865 283273. E-mail: richard.darton@eng.ox.ac.uk.

† Present address: Department of Chemical Engineering, Izmir Institute of Technology, Gulbahcekoyu Urla Izmir, Turkey 35430.

10.1021/ie049943l CCC: $27.50
Published on Web 07/13/2004

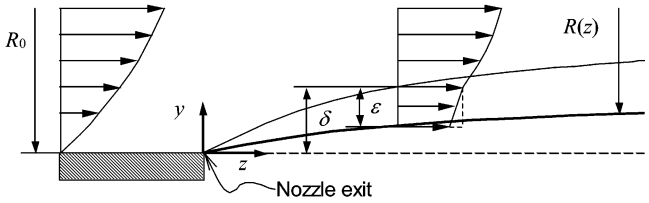

Figure 1. Development of the hydrodynamic boundary layer at the nozzle exit: R_0, nozzle radius; $R(z)$, jet radius; ϵ, thickness of the boundary layer (with contraction); δ, radial distance of the edge of the boundary layer from the nozzle wall; z, axial jet coordinate; y, Cartesian transverse coordinate in the boundary layer. A dashed line shows the boundary-layer velocity profile in the absence of surfactant ($\partial u/\partial y = 0$) and a solid line the boundary-layer velocity profile in the presence of surfactant ($\partial u/\partial y \neq 0$).

and computed results are presented. The following section presents our model of surfactant adsorption from an aqueous solution in the jet flow. The central diffusion−convection flux boundary condition at the free surface is discussed in detail, and the link between surfactant adsorption and the fluid mechanics in the jet (Marangoni flow) is highlighted. Finally, numerical results of surface coverage and dynamic surface tension for one surfactant (C_{16}TAB) at different concentrations are shown and validated through comparison with experimental data.

The combination of experimental, numerical, and analytical studies of the adsorption process in the jet flow leads to a validated surfactant adsorption model that is applicable to other types of free-surface flows on similar time scales, such as coating flows and the formation of foams. Such systems are not easily accessible for our experimental tools.

2. Asymptotic Behavior of the Jet Flow near the Nozzle Exit

2.1. Growth of the Zero-Vorticity Layer in the Absence of Surfactant: The Cube-Root Dependence. The velocity profile at the nozzle exit is that of fully developed laminar flow, with the usual no-slip condition at the wall. This no-slip condition is immediately relaxed when the fluid leaves the tube. In the absence of any surface shear (no surfactant present), a region of zero vorticity appears at the surface of the jet and, as the fluid travels downward, the zero-vorticity region diffuses toward the center of the jet, tending to equalize the velocity across the jet. Initially, however, this region is very thin, and we will consider its initial growth when its thickness, ϵ, is much less than the radius of the nozzle, R_0, or the jet, R (see Figure 1).

Near the jet nozzle, the effect of gravity may be neglected. Fluid in the zero-vorticity layer is accelerated by the adjacent layer of faster moving fluid. The parabolic profile at the nozzle exit ($z = 0$) is

$$U(y) = Ay + By^2 \tag{1}$$

where $A = 4\bar{u}_0 R_0^{-1}$ and $B = -2\bar{u}_0 R_0^{-2}$ and $\bar{u}_0$ is the mean jet velocity at the nozzle exit. At a distance z from the nozzle exit, the depth of the zero-vorticity layer, measured from the line $y = 0$, is δ. Note that the actual thickness of the layer, ϵ, is less than δ, as shown in Figure 1. If we let the axial velocity in the zero-vorticity layer be

$$u(y) = a + b\{y - (\delta - \epsilon)\} \tag{2}$$

then a is the axial surface velocity, u_s, and b is zero because there is no shear stress at the surface and so $\partial u/\partial y = 0$ throughout the layer. We set the condition that the velocity be continuous at the edge of the layer, so that $U(\delta) = u(\delta)$, which gives $A\delta + B\delta^2 = a$. Substituting for A, B, and a shows that the surface velocity is

$$u_s = 4\bar{u}_0\left(\frac{\delta}{R_0} - \frac{\delta^2}{2R_0^2}\right) \tag{3}$$

and, because $\delta \ll R_0$,

$$u_s = 4\bar{u}_0\delta/R_0 \tag{4}$$

The thickness of the layer, ϵ, at a distance z can be found by continuity, because

$$\int_0^\delta U(y)\,dy = \int_{\delta-\epsilon}^\delta u(y)\,dy \tag{5}$$

from which $A\delta^2/2 + B\delta^3/3 = a\epsilon$ and

$$\epsilon = \frac{2\bar{u}_0 R_0}{u_s}\left(\frac{\delta^2}{R_0^2} - \frac{\delta^3}{3R_0^3}\right) \tag{6}$$

and, because $\delta \ll R_0$,

$$\epsilon = \frac{2\bar{u}_0\delta^2}{u_s R_0} = \frac{\delta}{2} \tag{7}$$

The thickness of the vorticity-free layer is just half the distance δ.

The fluid streamlines that leave the nozzle between $y = 0$ and δ at a distance z are found between $y = \delta/2$ and δ. The rate of gain of momentum by the fluid in this layer is equal to the acting force. For unit width, assuming the depth of the layer is small compared with the jet radius, the rate of momentum gain is

$$\rho\int_0^\delta U(y)\left\{u\left(\frac{y+\delta}{2}\right) - U(y)\right\}dy = \mu\left(\frac{\partial U}{\partial y}\right)_{y=\delta} z \tag{8}$$

Neglecting terms in δ^3 and higher powers of δ, from eq 8 we obtain $Aa\delta^2 = 2\nu(A + 2B\delta)z$, so that $a = 2\nu(\delta^{-2} + 2BA^{-1}\delta^{-1})z$. From the parabolic profile, we have $2BA^{-1} = -R_0^{-1}$, so the surface velocity, $u_s = a$, is given by

$$u_s = \frac{2\nu z}{\delta^2}\left(1 - \frac{\delta}{R_0}\right) \tag{9}$$

and, because $\delta \ll R_0$,

$$u_s = 2\nu z/\delta^2 \tag{10}$$

Combining eqs 4 and 10 gives

$$u_s = \left(\frac{32\bar{u}_0^2\nu z}{R_0^2}\right)^{1/3} \tag{11}$$

$$\delta = \left(\frac{R_0\nu z}{2\bar{u}_0}\right)^{1/3} \tag{12}$$

and

$$\epsilon = \frac{1}{2}\left(\frac{R_0 \nu z}{2\bar{u}_0}\right)^{1/3} \tag{13}$$

The relative narrowing of the jet due to acceleration of the surface layer is given by

$$\frac{R(z)}{R_0} = \frac{R_0 - (\delta - \epsilon)}{R_0} = 1 - \frac{1}{2}\left(\frac{\nu z}{2{R_0}^2 \bar{u}_0}\right)^{1/3} \tag{14}$$

Introducing the dimensionless variables $u_s = u_s^* \bar{u}_0$ and $z = z^* R_0$ into eq 11 leads to

$$u_s^* = 4\left(\frac{z^*}{Re}\right)^{1/3} \tag{15}$$

where

$$Re \equiv \frac{2R_0 \rho \bar{u}_0}{\mu} = \frac{2R_0 \bar{u}_0}{\nu} \tag{16}$$

is the Reynolds number. Similarly, a dimensionless expression for the relative narrowing of the jet

$$R^* = \frac{R}{R_0} = 1 - 0.5\left(\frac{z^*}{Re}\right)^{1/3} \tag{17}$$

can be derived.

There is thus a singularity at the point ($z = 0$, $y = 0$) where the surface expansion rate, du_s/dz, becomes infinite. This singularity is a consequence of the step change in the surface shear condition at this point.

We note the connection to the classic *Graetz* heat-transfer problem in a circular tube,[7] where the thermal penetration depth in the thermal entry region of the flow scales as the axial distance raised to the $^1/_3$ power.

The cube-root dependence of u_s and R on z in liquid jets has been found by other authors. In the late 1950s, Scriven and Pigford investigated the absorption of CO_2 into freely falling laminar liquid jets.[8] They assumed a uniform velocity profile in the core of the jet (short nozzles were used, and hence a fully developed laminar flow was not achieved at the nozzle exit) and an annular boundary layer outside the core of the jet in which the velocity was reduced, because of viscous effects close to the nozzle wall. A cubic equation was employed to represent the velocity distribution within this annular boundary layer. Mass and momentum balances between the nozzle exit plane and a downstream position that corresponded to a fully relaxed velocity profile in the jet were carried out to estimate the boundary layer growth. The authors concluded from the smallness of the boundary layer at the nozzle—only $^1/_{10}$th of the nozzle radius—that the core velocity of the jet remained unchanged by momentum exchange with the boundary layer. If the rate of change of the jet diameter is negligibly small and gravity is neglected, the problem of analyzing the velocity distribution in the neighborhood of the jet surface is identical to the problem of calculating the velocity distribution in a laminar wake behind an infinitely thin, flat plate oriented parallel to the direction of flow. This analogy was pointed out earlier by Rideal and Sutherland.[9] The surface velocity near the nozzle exit was described by a cube-root dependence (at leading order) on the axial distance.

Goren studied the development of the boundary layer accompanying the formation of a free surface from a two-dimensional horizontal uniform shear flow that was taken to be of infinite extent in both directions.[10] When surface tension forces are neglected, his analysis shows that both the surface velocity and surface position vary with the cube root of the distance downstream. Goren's results are applicable to newly formed capillary jets for small axial distances, provided the interaction of the boundary layer with the core region of the jet, where the initial velocity profile is not one of uniform shear, is negligible. For a jet of average velocity $\bar{u}_0$, issuing from a long needle of radius R_0 with parabolic flow, Goren gave the equation for the dimensionless surface velocity, u_s^*, as

$$u_s^* = 5.07\left(\frac{z^*}{Re}\right)^{1/3} \tag{18}$$

and that for the dimensionless jet radius, R^*, as

$$R^* = 1 - 0.703\left(\frac{z^*}{Re}\right)^{1/3} \tag{19}$$

In the same year, Goren and Wronski reported measurements of the radius of horizontal capillary jets as a function of the axial distance.[11] For the highest Reynolds number under consideration ($Re \approx 200$), the measurements confirmed the cube-root dependence on the axial distance, but the observed coefficient was lower than the predicted one by about a factor of 2. The authors attributed this discrepancy to the smallness of the Reynolds number and possible interactions between the boundary layer and core fluid. It was suggested to test the boundary-layer analysis against experimental data at much higher Reynolds numbers of 1000−2000.

We have performed such a comparison in Figure 6 for $Re = 1950$, where both our eqs 15 and 17 are compared with the above results of Goren, eqs 18 and 19, and our own CFD model. The CFD data were compared with our experimental data in part 1 of this series of papers, where they were shown to be in excellent agreement.[6] In Figure 6, good agreement exists between the two boundary-layer treatments and the CFD computation for short jet lengths, where the effects of gravity and the interaction between the boundary layer and core fluid are negligibly small. The smallness of Re in the experiments of Goren and Wronski thus seems to be the likely cause of the disagreement with eq 19 in their study.

Only 2 years later, Tillett also applied boundary-layer analysis to a horizontal liquid jet emerging from a two-dimensional channel at high Reynolds number, but he assumed that the flow inside the channel has the basic Poiseuille profile.[12] Ignoring the effects of surface tension, Tillett did not confine modifications to the basic profile to the boundary layer. Instead, he derived solutions for the "inner" (boundary layer) region and the "outer" (core) region of the jet flow, which he matched. It emerged, however, from his solution that Goren's and Scriven and Pigford's assumption is fully justified: for moderate downstream distances, the interaction between the boundary layer and the core of the jet flow can be neglected, which also justifies the assumption that fully developed laminar flow exists at the channel/nozzle exit in the high Reynolds number limit. This assumption is otherwise inadequate as pointed out by Middleman,[13] Fisher et al.,[14] and Dutta and Ryan[15] in the course of their numerical investigations of creeping jet flows ($Re \approx 0$). Tillett confirmed Goren's solution for the channel flow (the cube-root dependence), but he did

not apply his derivations to the case of an axisymmetric jet leaving a circular pipe. At leading order, however, because the boundary layer is thin relative to the jet radius, these two problems are the same. Indeed, using Tillett's result for the surface velocity of the channel flow (eq 3.19 in the original work) and applying our normalizing scheme to it, we obtain the same result as that given by eqs 15 and 18 but with a factor of 5.11, which is nearly identical with Goren's result.

The cube-root dependence in the case of a jet of a pure liquid is thus a well-established result. We now go on to investigate how the presence of surfactant at the jet surface affects the boundary-layer development in the jet flow, particularly at the nozzle exit.

2.2. Growth of a Reduced-Vorticity Layer in the Presence of Surfactant. When a surfactant is present, its nonuniform surface concentration will give rise to a surface tension gradient: the Marangoni stress. The surface condition of the jet is no longer one of full slip, and the Marangoni stress gives rise to a velocity gradient in the layer adjacent to the surface, which is thus a region of reduced rather than zero vorticity. If this applied stress is τ_z at a distance z from the nozzle exit, then

$$\tau_z = -\mu \left(\frac{\partial u}{\partial y}\right)_{\text{surface}} \tag{20}$$

where for this approximate theory we have taken the coordinate y to be effectively perpendicular to the jet surface. If the velocity in the layer is again given by eq 2, then a is the surface velocity, u_s, and b is $-\tau_z/\mu$. The velocity profile in the core of the jet flow is not changed and is given by eq 1.

We set the condition that the velocity be continuous at the edge of the layer, so that $U(\delta) = u(\delta)$, which gives $A\delta + B\delta^2 = a + b\epsilon$. Substituting for A, B, a, and b shows that the surface velocity is

$$u_s = 4\bar{u}_0\left(\frac{\delta}{R_0} - \frac{\delta^2}{2{R_0}^2}\right) + \frac{\tau_z\epsilon}{\mu} \tag{21}$$

and, because $\delta \ll R_0$,

$$u_s = \frac{4\bar{u}_0\delta}{R_0} + \frac{\tau_z\epsilon}{\mu} \tag{22}$$

The thickness of the layer, ϵ, can be found by continuity. Applying eq 5, we have $A\delta^2/2 + B\delta^3/3 = a\epsilon + b\epsilon^2/2$. Hence

$$\frac{2\bar{u}_0R_0}{u_s}\left(\frac{\delta^2}{{R_0}^2} - \frac{\delta^3}{3{R_0}^3}\right) = \epsilon\left(1 - \frac{\tau_z\epsilon}{2\mu u_s}\right) \tag{23}$$

and, because $\delta \ll R_0$,

$$u_s = \frac{2\bar{u}_0\delta^2}{\epsilon R_0} + \frac{\tau_z\epsilon}{2\mu} \tag{24}$$

Combining eqs 22 and 24, we find the relation between δ and ϵ,

$$\delta^2 - 2\delta\epsilon - \frac{\tau_z}{4\mu\bar{u}_0/R_0}\epsilon^2 = 0 \tag{25}$$

The negative solution of eq 25 has no physical meaning, and the positive solution is

$$\delta = \left(1 + \sqrt{1 + \frac{\tau_z}{4\mu\bar{u}_0/R_0}}\right)\epsilon = \alpha\epsilon \tag{26}$$

The surface-slip factor α is in the range of $1 \leqslant \alpha \leqslant 2$ because τ_z is in general a negative quantity. The lower limit represents a no-slip condition at the jet surface, and the upper limit represents the stress-free surface analyzed previously. The term $4\mu\bar{u}_0/R_0$ is the shear stress at the nozzle wall, which results from the parabolic flow profile.

The rate of gain of momentum by fluid in the layer is equal to the force acting on the layer, which this time must include the surface tension. Again when gravity is neglected and it is assumed that the depth of the layer is small compared with the jet radius, the rate of momentum gain per unit width is

$$\rho\int_0^\delta U(y)\left\{u\left(\frac{\epsilon y}{\delta} + \delta - \epsilon\right) - U(y)\right\}\mathrm{d}y = \mu\left(\frac{\partial U}{\partial y}\right)_{y=\delta} z + (\sigma_z - \sigma_0) \tag{27}$$

where σ_0 is the surface tension at the nozzle exit and σ_z is the surface tension at the distance z. In this balance we have discounted the fact that the jet surface is not cylindrical and therefore that the surface tensions do not quite act in the z direction and that the tension σ_z acts over a slightly smaller perimeter than σ_0 does. In the high Reynolds number limit, this simplification is made at little expense.

Again neglecting terms in δ^3 and higher powers of δ, we obtain $Aa\delta^2/2 = \nu(A + 2B\delta)z + (\sigma_z - \sigma_0)/\rho$, so that

$$a = \frac{2\nu z}{\delta^2}\left(1 - \frac{\delta}{R_0}\right) + \frac{R_0\Delta\sigma}{2\rho\bar{u}_0\delta^2} \tag{28}$$

where $\Delta\sigma = \sigma_z - \sigma_0$ is the change in the surface tension over the distance z. Because $\delta \ll R_0$, the surface velocity, $u_s = a$, is given by

$$u_s = \frac{2\nu z}{\delta^2} + \frac{R_0\Delta\sigma}{2\rho\bar{u}_0\delta^2} \tag{29}$$

We can use eqs 22 and 26 to eliminate δ from eq 29 and find the surface velocity as

$$u_s = \left(\frac{32{\bar{u}_0}^2\nu z}{{R_0}^2}\right)^{1/3}\left(1 + \frac{\Delta\sigma/z}{4\mu\bar{u}_0/R_0}\right)^{1/3}\left(1 + \frac{\tau_z/\alpha}{4\mu\bar{u}_0/R_0}\right)^{2/3} \tag{30}$$

which can be rearranged to give

$$u_s = \left(\frac{32{\bar{u}_0}^2\nu z}{{R_0}^2}\right)^{1/3}\left(1 + \frac{\Delta\sigma/z}{4\mu\bar{u}_0/R_0}\right)^{1/3}\left(1 + \frac{\tau_z}{4\mu\bar{u}_0/R_0}\right)^{1/3} \tag{31}$$

Both the mean Marangoni stress $\Delta\sigma/z$ and the local value at z, $\tau_z = \mathrm{d}\sigma/\mathrm{d}z$, will in general be negative quantities, so that the result, as expected, is a reduction in the surface velocity from what it would be in the absence of the surfactant. Note that, within a boundary-layer treatment, the Marangoni stress in the jet is $\mathrm{d}\sigma/\mathrm{d}z \geqslant -4\mu\bar{u}_0/R_0$, which is equal to the stress value inside the nozzle. We use this condition in the numerical

computations to limit the Marangoni stress at $z = 0$. Later, we discuss briefly the physical consequences of relaxing this restriction on $d\sigma/dz$.

The corresponding values of δ and ϵ are

$$\delta = \left(\frac{R_0 \nu z}{2\bar{u}_0}\right)^{1/3}\left(1 + \frac{\Delta\sigma/z}{4\mu\bar{u}_0/R_0}\right)^{1/3}\left(1 + \frac{\tau_z}{4\mu\bar{u}_0/R_0}\right)^{-1/6} \quad (32)$$

and

$$\epsilon = \delta/\alpha \quad (33)$$

where the surface-slip factor α is defined in eq 26. The relative narrowing of the jet due to acceleration of the surface layer is given by

$$\frac{R(z)}{R_0} = \frac{R_0 - (\delta - \epsilon)}{R_0} = 1 - \frac{1}{\alpha}\left(\frac{\nu z}{2{R_0}^2\bar{u}_0}\right)^{1/3}\left(1 + \frac{\Delta\theta/z}{4\mu\bar{u}_0/R_0}\right)^{1/3}\left(1 + \frac{\tau_z}{4\mu\bar{u}_0/R_0}\right)^{1/3} \quad (34)$$

We can again derive dimensionless expressions, $u_s^* = u_s^*(z^*)$ and $R^* = R^*(z^*)$, for the surface velocity and the radius of the jet, respectively. With our definitions for u_s^* and z^*, eq 31 may be rewritten to give

$$u_s^* = \left(\frac{64z^*}{Re}\right)^{1/3}\left[1 + \frac{(\sigma_z - \sigma_0)}{4z^*\mu\bar{u}_0}\right]^{1/3}\left(1 + \frac{\tau_z R_0}{4\mu\bar{u}_0}\right)^{1/3} \quad (35)$$

Defining the Capillary number, Ca, as $\mu\bar{u}_0/\sigma$, and

$$Ma \equiv \left|\frac{1}{Ca} - \frac{1}{Ca_0}\right| = \frac{|\sigma_z - \sigma_0|}{\mu\bar{u}_0} \quad (36)$$

where Ma is the Marangoni number, and introducing $\tau_z = d\sigma/dz$, we get

$$u_s^* = \left(\frac{64z^*}{Re}\right)^{1/3}\left(1 - \frac{Ma}{4z^*}\right)^{1/3}\left[1 + \frac{1}{4}\frac{d}{dz^*}\left(\frac{1}{Ca}\right)\right]^{1/3} \quad (37)$$

Correspondingly, the dimensionless radius of the jet is

$$R^* = 1 - \frac{1}{\alpha}\left(\frac{z^*}{Re}\right)^{1/3}\left(1 - \frac{Ma}{4z^*}\right)^{1/3}\left[1 + \frac{1}{4}\frac{d}{dz^*}\left(\frac{1}{Ca}\right)\right]^{1/3} \quad (38)$$

In our expression for the surface velocity, eq 37, we included terms for the Marangoni stress: the mean Marangoni stress Ma/z^* and the local value $d/dz^*\,(1/Ca)$. This stress cannot be determined from the dynamics of the jet because it depends on the surface concentration, which, in turn, depends on the diffusion of the surfactant to the surface. To solve the jet dynamics fully, we must also solve the coupled mass-transfer problem. The set of equations that describes the coupled problem is too complex for analytical solution and must be tackled using CFD methods. However, it is useful to derive some approximate results so as to understand the shape of the problem and the features displayed by the computed solution. We derive these approximate results by dividing the jet flow into two zones, the downstream jet flow and the flow of the jet near the nozzle, which we term the detachment region, with the nozzle exit at $z^* = 0$ being the point of detachment.

2.3. Downstream Jet Flow. Diffusion occurs when expansion of the surface, $du_s^*/dz^* = f'(z^*)$, reduces the subsurface concentration, $w_s = w(y^* = 0, z^*)$, of the surfactant below its equilibrium level. Note that in this section on modeling the mass transfer we take y^* to be measured from the surface of the jet. The subsurface concentration is given as a mass fraction, $w_s = (M/\rho)c_s$, where c_s is the molar concentration at the subsurface and M is the molecular weight of the surfactant. We note first that the thickness of the diffusion boundary layer will be small compared with the thickness of the hydrodynamic boundary layer, so that diffusion may be assumed to be taking place within a layer moving with the surface velocity, $u_s^* = f(z^*)$, throughout its depth. Within the diffusional boundary layer, there is a velocity v^* perpendicular to the surface where by continuity (neglecting curvature and contraction of the jet)

$$\frac{\partial u_s^*}{\partial z^*} + \frac{\partial v^*}{\partial y^*} = 0 \leftrightarrow -f'(z^*) = \frac{\partial v^*}{\partial y^*} \quad (39)$$

This relationship shows that the velocity gradient within the diffusion boundary layer, $\partial v^*/\partial y^*$, is determined by variation in the surface velocity, $f'(z^*)$. We can integrate eq 39 to find

$$v^* = -y^* f'(z^*) \quad (40)$$

because v^* is zero at the surface ($y^* = 0$), and the streamwise velocity can be taken not to vary over the very thin boundary layer, at given z^*.

The convection−diffusion equation, in its dimensionless form, is

$$\frac{\partial^2 w}{\partial {y^*}^2} + \frac{Re}{2}Scy^* f'(z^*)\frac{\partial w}{\partial y^*} = \frac{Re}{2}Scu_s^*\frac{\partial w}{\partial z^*} \quad (41)$$

In eq 41, the Schmidt number, Sc, is defined as

$$Sc \equiv \mu/\rho D \quad (42)$$

where D is the coefficient of diffusivity of surfactant molecules in water.

The Péclet number, $Pe \equiv (Re \times Sc)/2 = R_0\bar{u}_0/D$, is $\mathcal{O}(10^6) \gg 1$. This indicates that we can neglect the contribution of axial diffusion in eq 41. This simplification is valid throughout the fluid, except very close to the point of detachment, where the surface concentration (and hence the subsurface concentration) changes rapidly and the surface velocity is low.

It may be shown that the transverse convection term in eq 41 scales as $z^{*-2/3}$, whereas the axial convection term (right-hand side of eq 41) scales as $z^{*-1/3}$. We are particularly interested in the solution of eq 41 near to the nozzle, where the axial convection term is relatively small. In this simplified model, we therefore ignore the axial convection term in eq 41.

The boundary conditions are that $w = w_s$ at $y^* = 0$ and $w \to w_b$ as $y^* \to \infty$, where w_b is the bulk concentration and w_s is the subsurface concentration. The solution of eq 41 is

$$\frac{w - w_s}{w_b - w_s} = \mathrm{erf}\left\{\frac{y^*}{2}\sqrt{Re \times Scf'(z^*)}\right\} \quad (43)$$

Table 1. Parameters $\mathscr{C}$ and m of the Power-Law Fit, Eq 107, as a Function of the Bulk Concentration, c_b, of C_{16}TAB for $Re = 1950$, Estimated Surface Concentration at the Point of Detachment Γ_0^*, Eq 74, and the Corresponding Values of the Subsurface Concentration $w_{s,0}$, Eq 100, as a Function of c_b

c_b/(mol m^{-3})	$w_b/\times 10^{-6}$	$\mathscr{C}$	m	Γ_0^*	$w_{s,0}/\times 10^{-6}$
0.01	3.645	2.32×10^{-7}	0.2910	0.0002	0.0125
0.05	18.225	1.17×10^{-6}	0.2974	0.0017	0.1396
0.10	36.450	2.34×10^{-6}	0.3054	0.0048	0.3962
0.30	109.350	7.25×10^{-6}	0.3383	0.0249	2.1009
0.63	229.635	1.67×10^{-5}	0.3840	0.0757	6.7451
0.90	328.050	2.79×10^{-5}	0.3965	0.1293	12.2256

Table 2. Values of Physical Parameters Used in the Numerical Computation

R_0	nozzle radius	0.79×10^{-3} m
$\bar{u}_0$	mean nozzle exit velocity	1.236 m s^{-1}
ρ	density of water	10^3 kg m^{-3}
μ	viscosity of water	10^{-3} kg m^{-1} s^{-1}
σ_w	surface tension of water	72.8×10^{-3} N m^{-1}
M	molecular weight of C_{16}TAB	364.5×10^{-3} kg mol^{-1}
k	Langmuir constant of C_{16}TAB	0.23 mol m^{-3}
Γ_{sat}	saturation surface coverage of C_{16}TAB	3.9×10^{-6} mol m^{-2}
D	diffusivity of C_{16}TAB	7.46×10^{-10}m^2 s^{-1}
N	ionic number of C_{16}TAB	2
$\mathscr{R}$	universal gas constant	8.314 J mol^{-1} K^{-1}
T	temperature	293.15 K
g	gravity	9.81 m s^{-2}

in which $f'(z^*) = \mathrm{d}u_s^*/\mathrm{d}z^*$ is the rate of expansion of the jet surface.

We note that there is a similarity solution to the complete eq 41, which is identical with eq 43 with the exception that the argument of the error function is increased by a factor of $\sqrt{2}$. This similarity solution may be found by taking w to be a function of the similarity variable $y^*z^{*-1/3}$ (see work by Deen,[7] p 382).

The dimensionless diffusion mass flux to the surface, defined as $q_{s,diff}^* = q_{s,diff}R_0(\rho D)^{-1}$, is given by

$$q_{s,diff}^* = \left(\frac{\partial w}{\partial y^*}\right)_{y^*=0} = [w_b - w_s(z^*)]\sqrt{\frac{Re \times Sc}{\pi}\frac{\mathrm{d}u_s^*}{\mathrm{d}z^*}} \quad (44)$$

Diffusion to the surface of the jet is balanced by convection in the surface (see work by Levich,[16] p 393). When the (small) change in the perimeter of the jet is neglected, this dimensionless convective surface flux, $q_{s,conv}^* = q_{s,conv}R_0(\rho D)^{-1}$, is given as

$$q_{s,conv}^* = \frac{M\bar{u}_0\Gamma_{sat}}{\rho D}\left\{\frac{\mathrm{d}}{\mathrm{d}z^*}(u_s^*\Gamma^*) + \frac{2}{Re \times Sc_s}\frac{\mathrm{d}^2\Gamma^*}{\mathrm{d}z^{*2}}\right\} \quad (45)$$

where the term $2(Re \times Sc_s)^{-1}\ \mathrm{d}^2\Gamma^*/\mathrm{d}z^{*2}$ accounts for diffusion in the surface, which accompanies the convection $\mathrm{d}/\mathrm{d}z^*\ (u_s^*\Gamma^*)$. Sc_s is the Schmidt number in the surface, which contains the diffusivity of monomers in the surface, D_s. If we assume that $D_s = D$, u_s^* is given by eq 15, and $\Gamma^* \sim z^{*1/3}$, we find that the surface diffusion contribution is negligibly small compared with the surface convection for the values of the physical parameters given in Table 2. Therefore, we do not consider the surface diffusion contribution any further.

In eq 45, $\Gamma^* = \Gamma/\Gamma_{sat}$ is the dimensionless surface concentration or surface coverage. We note that the saturation surface concentration, Γ_{sat}, is a value deduced from the equilibrium adsorption isotherm, as $w_b \to \infty$. In practice, the maximum surface concentration, observed as the bulk concentration reaches the critical micelle concentration (cmc), is less than Γ_{sat}. For C_{16}TAB, this maximum value is about $0.8\Gamma_{sat}$.

If the Marangoni stresses are small compared with the maximum value at the nozzle exit, then we can assume that the surface velocity has the surfactant-free value. This will be the case for dilute solutions, some way from the nozzle exit. In this case, the surface velocity, $u_s^* = u_s^*(z^*)$, is given by eq 15. Substituting for the surface expansion, $\mathrm{d}u_s^*/\mathrm{d}z^*$, in eq 44 and assuming that the subsurface concentration remains low compared to the concentration in the bulk, $w_b - w_s \approx w_b$, gives

$$q_{s,diff}^* = \left(\frac{Re \times Sc}{\pi}\right)^{1/2}\left(\frac{64}{27Re}\right)^{1/6} w_b z^{*-1/3} \quad (46)$$

The surface concentration, $\Gamma^* = \Gamma^*(z^*)$, can be found by balancing convection and diffusion at the surface (eqs 45 and 46)

$$\left(\frac{Re \times Sc}{\pi}\right)^{1/2}\left(\frac{64}{27Re}\right)^{1/6} w_b \int_0^{z^*} z^{*-1/3}\,\mathrm{d}z^* = \frac{M\bar{u}_0\Gamma_{sat}}{\rho D}\int_0^{z^*} \mathrm{d}(u_s^*\Gamma^*) \quad (47)$$

and with eq 15 for u_s^*, we find

$$\Gamma^* = 0.244\left(\frac{\rho D}{M\bar{u}_0\Gamma_{sat}}\right)Re^{2/3}Sc\,w_b z^{*1/3} \quad (48)$$

when the Marangoni stress is small.

For low concentrations, the variation in the surface tension, $\mathrm{d}/\mathrm{d}z^*\ (1/Ca)$, is obtained from a surface equation of state, Henry's law, which relates the surface tension to the surface concentration

$$\frac{1}{Ca} = \frac{1}{Ca_w} - \frac{N\mathscr{R}T\Gamma_{sat}}{\mu\bar{u}_0}\Gamma^* \quad (49)$$

This gives

$$\frac{\mathrm{d}}{\mathrm{d}z^*}\left(\frac{1}{Ca}\right) = -\frac{N\mathscr{R}T\Gamma_{sat}}{\mu\bar{u}_0}\frac{\mathrm{d}\Gamma^*}{\mathrm{d}z^*} \quad (50)$$

and, with $\mathrm{d}\Gamma^*/\mathrm{d}z^*$ from eq 48,

$$\frac{\mathrm{d}}{\mathrm{d}z^*}\left(\frac{1}{Ca}\right) = -\frac{E}{12.28}\left(\frac{\rho D}{M\bar{u}_0\Gamma_{sat}}\right)Re^{2/3}Sc^{1/2}w_b z^{*-2/3} \quad (51)$$

where

$$E \equiv N\mathscr{R}T\Gamma_{sat}/\mu\bar{u}_0 \quad (52)$$

is the Elasticity number. It is a measure of the importance of the surface tension change caused by surfactant adsorption relative to the viscous force. In eq 52, N reflects the number of ions delivered to the surface by a molecule of surfactant ($N = 1$ for nonionics, $N = 2$ for ionics with monovalent ions, etc.), $\mathscr{R}$ is the universal gas constant, and T is the temperature.

Both the surface concentration and the surface tension will vary approximately with the $^1/_3$ power of distance from the nozzle, that is, $\Gamma^* \sim z^{*1/3}$ and $Ca^{-1} \sim z^{*1/3}$, respectively. This implies that $\mathrm{d}\Gamma^*/\mathrm{d}z^* \sim z^{*-2/3}$ and

$d/dz^*\,(1/Ca) \sim z^{*-2/3}$, from which it follows that $d\Gamma^*/dz^* \to \infty$ and $d/dz^*\,(1/Ca) \to \infty$ as $z^* \to 0$. This behavior contravenes our assumption that the Marangoni stress is small, so that the cube-root dependence of eq 48 must break down as $z^* \to 0$.

The derivations made in this section apply to the region of the jet flow, where the Marangoni stress is small compared to the maximum shear stress at the nozzle exit, that is, outside the region of detachment (see the next section) but still close enough to the nozzle exit for the assumptions of low concentration (Henry's law) and neglect of gravity and streamwise convection in the boundary layer to be valid.

2.4. Flow near the Nozzle: The Detachment Region. It is important for the description of flow further down the jet to know how the jet surface moves immediately after it detaches from the nozzle. In particular, we wish to establish the conditions under which acceleration of the liquid at the point of detachment remains finite and what the surface concentration is near the nozzle.

2.4.1. Surface Velocity and Surface Concentration. The surface concentration gradient at the point of detachment, $d\Gamma^*/dz^*$ at $z^* = 0$, must remain finite and sufficiently small that the maximum Marangoni stress, $4\mu\bar{u}_0/R_0$, consistent with a boundary-layer treatment of the hydrodynamics is not exceeded. Considering the fluxes from eqs 44 and 45, we see that if they are to match each other, we must have $(du_s^*/dz^*)^{1/2} \sim d(u_s^*\,\Gamma^*)/dz^*$. If we suppose that u_s^* varies as z^{*n} ($n > 0$) to leading order, then Γ^* must vary as $z^{*(1-n)/2}$ as $z^* \to 0$. Because Γ^* remains finite as $z^* \to 0$, $n \leq 1$. However, near the nozzle a value of n of less than unity is precluded because $d\Gamma^*/dz^*$ must remain finite as $z^* \to 0$. Hence, $n = 1$ and the leading order term in a Taylor expansion for Γ^* about $z^* = 0$ is a constant value $\Gamma_0^* = \Gamma_0/\Gamma_{sat}$. Near the nozzle, the surface velocity increases linearly with distance and the surface acceleration at $z^* = 0$ is finite.

From eq 37, near the nozzle,

$$u_s^* = \left(\frac{64z^*}{Re}\right)^{1/3}\left(1 - \frac{Ma}{4z^*}\right)^{1/3}\left[1 + \frac{1}{4}\frac{d}{dz^*}\left(\frac{1}{Ca}\right)\right]^{1/3} \sim \kappa z^* \quad (53)$$

where κ is a constant that is to be determined. It emerges from eq 53 that as $z^* \to 0$, where we have $-Ma(4z^*)^{-1} = d/dz^*\,(4Ca)^{-1}$, if the surface acceleration is to remain finite, we must have

$$\left\{\frac{d}{dz^*}\left(\frac{1}{Ca}\right)\right\}_{z^*=0} = \left\{\frac{d}{dz^*}\left(\frac{1}{Ca}\right)\right\}_{max} = -4 \quad (54)$$

The local Marangoni stress must have its maximum (negative) value at that point. We note that this result is independent of the concentration of the surfactant. We can integrate eq 53 to obtain the dependence of the surface tension parameter, Ca^{-1}, on the axial distance, z^*, near the origin. We obtain

$$\frac{1}{Ca} = \frac{1}{Ca_0} - 4z^* + \frac{\kappa^{3/2}\sqrt{Re}}{4}z^{*2} \quad (55)$$

which is valid as $z^* \to 0$. From eq 55, we obtain for the Marangoni stress in the detachment region

$$\frac{d}{dz^*}\left(\frac{1}{Ca}\right) = -4 + \frac{\kappa^{3/2}\sqrt{Re}}{2}z^* \quad (56)$$

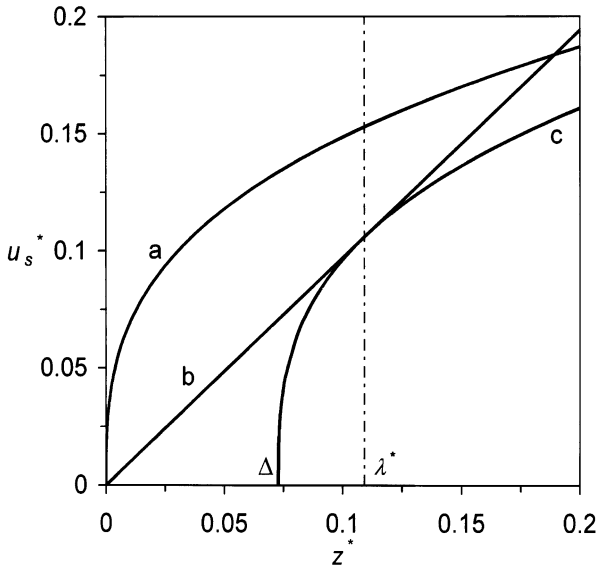

Figure 2. Definition of the length of the detachment region, λ^*. Data are for $Re = 1950$ and $c_b = 0.3$ mol m^{-3} C_{16}TAB in water. Curve a is u_s^* of the surfactant-free jet, given by eq 15. Curve b is u_s^* in the region of detachment, given by eq 61. Curve c is u_s^* of the jet in the presence of surfactant outside the region of detachment, given by eq 62.

We can now derive the expression for the dependence of the surface coverage, Γ^*, on z^* in the region of detachment using Henry's law, eq 50, and eq 56. We obtain through integration

$$\Gamma^* = \Gamma_0^* + \frac{4}{E}z^* - \frac{\kappa^{3/2}\sqrt{Re}}{4E}z^{*2} \quad (57)$$

2.4.2. Matching with the Far-Field Solution. We have thus shown that there is a (short) detachment region in which the surface velocity increases linearly from zero at $z^* = 0$ and a region further from the nozzle in which, according to eq 15, the surface velocity varies with the cube root of the distance, as the Marangoni stress becomes negligible. We can estimate the length scale of the detachment region, $\lambda^* = \lambda/R_0$, which is defined as the length at which the detachment region solution and the far-field solution both exhibit the same surface velocity, u_s^*, and the same surface expansion, du_s^*/dz^*, in the following way (see Figure 2).

The upward Marangoni stress near the nozzle acts so as to reduce the surface velocity in the downstream region slightly. This velocity reduction may be considered equivalent to a small displacement of the nozzle exit, say Δ, in a downward sense. Suppose that for large values of z^*, from eq 15,

$$u_s^* = \left(\frac{64}{Re}\right)^{1/3}(z^* - \Delta)^{1/3} \quad (58)$$

which is valid for $z^* \geq \Delta$ (curve c in Figure 2). In eq 58, we can approximate $(z^* - \Delta)^{1/3} \approx z^{*1/3} - (\Delta/3)z^{*-2/3}$, so that for $z^* \to \infty$ we see that $(z^* - \Delta)^{1/3} \to z^{*1/3}$. The Marangoni effect thus vanishes as the jet travels downstream, and for $z^* \to \infty$, eq 58 becomes eq 15, which is given by curve a in Figure 2. For small z^*, we assume that u_s^* shows linear behavior according to eq 53, which is demonstrated by curve b in Figure 2. We

match both u_s^* and du_s^*/dz^* at $z^* = \lambda^*$, from which we obtain

$$\Delta = \frac{2}{3}\lambda^* \tag{59}$$

and

$$\kappa = \left(\frac{64}{3Re}\right)^{1/3}\lambda^{*-2/3} \tag{60}$$

The velocity profiles are thus given by

$$u_s^* = \left(\frac{64}{3Re}\right)^{1/3}\lambda^{*-2/3}z^* \tag{61}$$

in the region of detachment and

$$u_s^* = \left(\frac{64}{Re}\right)^{1/3}\left(z^* - \frac{2}{3}\lambda^*\right)^{1/3} \tag{62}$$

in the downstream region.

The solutions for the surface concentration, Γ^*, in the downstream region and in the region of detachment, eqs 48 and 57, respectively, are matched using a procedure similar to that used for the matching of the surface velocity. As before, we introduce an offset value into the downstream solution for Γ^*. This offset value, say $\tilde{\Delta}$, is different from Δ.

Equation 48 then becomes

$$\Gamma^* = \mathscr{A}(z^* - \tilde{\Delta})^{1/3} \tag{63}$$

where

$$\mathscr{A} = 0.244\left(\frac{\rho D}{M\bar{u}_0\Gamma_{sat}}\right)Re^{2/3}Sc^{1/2}w_b \tag{64}$$

We match the values Γ^* and the slopes $d\Gamma^*/dz^*$ from eqs 63 and 57 at $z^* = \lambda^*$, which gives

$$\Gamma_0^* + \left(2 - \frac{1}{\sqrt{3}}\right)\frac{2\lambda^*}{E} = \mathscr{A}(\lambda^* - \tilde{\Delta})^{1/3} \tag{65}$$

and

$$\frac{\mathscr{A}}{3}(\lambda^* - \tilde{\Delta})^{-2/3} = \frac{4}{E}\left(1 - \frac{1}{\sqrt{3}}\right) \tag{66}$$

respectively. From eq 66, we find directly for the offset value

$$\tilde{\Delta} = \lambda^* - \left[\frac{12}{E\mathscr{A}}\left(1 - \frac{1}{\sqrt{3}}\right)\right]^{-3/2} \tag{67}$$

The matching of the two solutions for Γ^* at $z^* = \lambda^*$ is shown graphically in Figure 3. The downstream solution for Γ^* without the offset value $\tilde{\Delta}$, eq 48, is given by curve a, and curve b represents the solution for Γ^* in the region of detachment, eq 57. Curve c is the downstream solution for Γ^*, which is shifted in the axial direction by the offset value $\tilde{\Delta}$, eq 63. We see from Figure 3 that the offset value $\tilde{\Delta}$ is a negative quantity. The reduced surface velocity decreases the convection in the surface. For the convective surface flux, $u_s^*\Gamma^*$, to balance diffusion of surfactant to the surface, requires that Γ^* increases. Thus, it appears downstream that the source of the jet has moved a distance $\tilde{\Delta}$ upstream, as shown

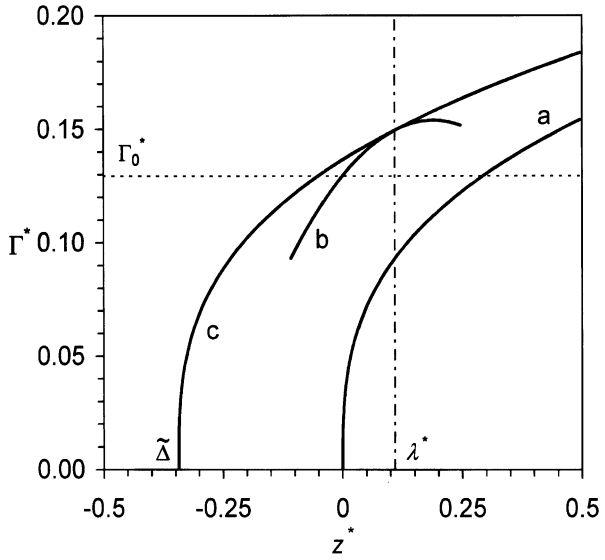

Figure 3. Matching of the solutions for Γ^* in the region of detachment (curve b, eq 57) and in the downstream region, where curve a, given by eq 48, is the downstream solution for Γ^* if the surface velocity of the surfactant-free jet is assumed, and curve c, given by eq 63, is the downstream solution for Γ^* with the reduced surface velocity of the jet in the presence of surfactant. Data are for $Re = 1950$ and $c_b = 0.9$ mol m^{-3} C_{16}TAB in water.

in Figure 3. The matched solution for Γ^* consists of curve b on the interval $0 \leq z^* \leq \lambda^*$ and curve c for $z^* \geq \lambda^*$.

2.4.3. Calculating λ^* and Γ_0^*. Using eq 67 to replace $\tilde{\Delta}$ in eq 65, we find a quadratic equation that contains λ^* and Γ_0^*, namely

$$\Gamma_0^{*2} + \left(2 - \frac{1}{\sqrt{3}}\right)\frac{4\lambda^*}{E}\Gamma_0^* + \left[\left(2 - \frac{1}{\sqrt{3}}\right)\frac{2\lambda^*}{E}\right]^2 = \frac{E\mathscr{A}^3}{12}\left(1 - \frac{1}{\sqrt{3}}\right)^{-1} \tag{68}$$

which has the solution

$$\Gamma_0^* = -\frac{5.6906\lambda^*}{2E} \pm \sqrt{\frac{E\mathscr{A}^3}{5.0718}} \tag{69}$$

Only the positive solution in eq 69 has a physical meaning.

We have thus found a relation between the length of the detachment region, λ^*, and the surface concentration at the point of detachment, Γ_0^*. Both λ^* and Γ_0^* are still unknown, and a second relation is needed to determine them. Intuitively, it may seem that this second relation could be obtained from the matching of the solutions for the surface tension parameter, Ca^{-1}, which are given by eqs 49 and 48 in the downstream region and by eq 55 in the region of detachment, in a way that is analogous to the matching of the surface concentration, but that is, in fact, not the case. Indeed, if we carry out this matching procedure, we find that the downstream solution for Ca^{-1} is offset by a value that equals exactly $\tilde{\Delta}$. This is a consequence of using a linear equation of state.

The second relation for λ^* and Γ_0^* is found from a mass balance around the surface at the point of detachment. Balancing diffusion and convection at $z^* = 0$, eqs 44 and 45, where we assume that $w_b \gg w_{s,0} = w_s$ ($z^* = 0$), and using the detachment region solution for

u_s^*, eq 61, gives

$$\Gamma_0^* = \mathscr{A}\frac{0.3388}{0.244}\lambda^{*1/3} \tag{70}$$

Setting eqs 69 and 70 equal gives an equation for λ^*

$$\mathscr{A}\frac{0.3388}{0.244}\lambda^{*1/3} + \frac{2.8453}{E}\lambda^* = \frac{(E\mathscr{A}^3)^{1/2}}{2.2521} \tag{71}$$

Equation 71 is a reduced cubic equation, for which the solution can be found by standard procedures, and is

$$\lambda^* = 0.0211(E\mathscr{A})^{3/2} \tag{72}$$

Resubstituting for $\mathscr{A}$ gives

$$\lambda^* = 2.543 \times 10^{-3}\left(E\frac{\rho D}{M\bar{u}_0\Gamma_{sat}}\right)^{3/2} Re \times Sc^{3/4} {w_b}^{3/2} \tag{73}$$

At first sight, it may seem surprising that the surface acceleration at the point of detachment is fundamentally changed by the presence of surfactant because this might suggest that the no-surfactant case is not obtained by reducing the surfactant concentration toward zero. In fact, a steady reduction of the surfactant concentration, w_b, reduces the length of the detachment region, λ^*, and increases the surface acceleration at the point of detachment. Taking the value of λ^* from eq 73 shows that $du_s^*/dz^* \sim \lambda^{*-2/3} \sim {w_b}^{-1}$, which gives $du_s^*/dz^* \rightarrow \infty$ as $w_b \rightarrow 0$, so that the limiting (pure water) case emerges correctly.

Replacing λ^* in eq 70 with eq 73 and resubstituting for $\mathscr{A}$, we find

$$\Gamma_0^* = 0.0462E^{1/2}\left(\frac{\rho D}{M\bar{u}_0\Gamma_{sat}}\right)^{3/2} Re \times Sc^{3/4} {w_b}^{3/2} \tag{74}$$

The surface concentration at the point of detachment and the length of the detachment region thus show the same dependence on the bulk concentration.

The simplified theory shows that $(du_s^*/dz^*)_{z^*=0}$ is finite when surfactant is present. This is an important result, which may be contrasted with the no-surfactant case in which $(du_s^*/dz^*)_{z^*=0}$ is infinite. In a related result, the simplified theory also shows that when surfactant is present, there is a finite amount, Γ_0^*, which may be small, adsorbed at the surface of the jet at the point of detachment.

2.5. Region of Validity. We have assumed in the analysis that $\delta \ll R_0$, which, using the result for a pure water jet, means that

$$\left(\frac{\nu z}{2\bar{u}_0 {R_0}^2}\right)^{1/3} \ll 1, \quad \text{or } z^* = \frac{z}{R_0} \ll Re \tag{75}$$

Our experiments have been carried out at $1000 \leqslant Re \leqslant 2000$, and this condition on z^* is easily fulfilled over that part of the jet on which experiments are made.

We have also neglected gravity, which in practice serves to accelerate the jet. Our derivation is thus valid provided that gravity does not affect the vorticity-free layer

$$u_s\frac{du_s}{dz} \gg g \tag{76}$$

where g is the acceleration due to gravity. Using the results for a pure water jet, this condition is

$$\left(\frac{32{\bar{u}_0}^2\nu z}{{R_0}^2}\right)^{1/3}\left(\frac{32{\bar{u}_0}^2\nu}{27{R_0}^2 z^2}\right)^{1/3} \gg g, \quad \text{or } z^* = \frac{z}{R_0} \ll \frac{32^3 Fr^3}{27Re^2} \tag{77}$$

where

$$Fr \equiv \frac{{\bar{u}_0}^2}{2R_0 g} \tag{78}$$

is the Froude number. We also require the bulk of the jet itself to be unaffected by gravity, so

$${\bar{u}_0}^2 \gg 2gz, \quad \text{or } z^* \ll Fr \tag{79}$$

The Froude numbers in our experiments are in the range of $50 \leqslant Fr \leqslant 100$, so that the latter condition is likely to be the more restrictive.

We have also assumed in the mass-transfer model that the surface concentration remains far below saturation and that in the vicinity of the nozzle the concentration is low enough for Henry's law to be applied to the surface phase.

3. Fluid Mechanics of the Jet Flow

3.1. Governing Partial Differential Equations. The numerical treatment of the hydrodynamics of laminar jets of pure liquids at high Reynolds numbers received considerable attention during the late 1970s and throughout the 1980s.[17,18] In this paper, we obtain the flow field of the jet using FIDAP, one of FLUENT's general-purpose CFD solvers that employs a finite-element method to discretize the governing set of partial differential equations.

The three-dimensional liquid jet is reduced to the axisymmetric case. The origin of the cylindrical coordinate system is located on the center (symmetry) line of the jet in the nozzle exit plane. Gravity points in the positive axial direction (see Figure 4). The Navier–Stokes equations and the equation of continuity are solved in their dimensionless forms, which are

$$v^*\frac{\partial u^*}{\partial r^*} + u^*\frac{\partial u^*}{\partial z^*} = -\frac{\partial p^*}{\partial z^*} + \frac{2}{Re}\left(\frac{1}{r^*}\frac{\partial}{\partial r^*}\left(r^*\frac{\partial u^*}{\partial r^*}\right) + \frac{\partial^2 u^*}{\partial z^{*2}}\right) + \frac{1}{2Fr} \tag{80}$$

$$v^*\frac{\partial v^*}{\partial r^*} + u^*\frac{\partial v^*}{\partial z^*} = \frac{\partial p^*}{\partial r^*} + \frac{2}{Re}\left[\frac{\partial}{\partial r^*}\left(\frac{1}{r^*}\frac{\partial}{\partial r^*}(r^*v^*)\right)\right] + \frac{\partial^2 v^*}{\partial z^{*2}} \tag{81}$$

and

$$\frac{1}{r^*}\frac{\partial}{\partial r^*}(r^*v^*) + \frac{\partial u^*}{\partial z^*} = 0 \tag{82}$$

respectively. The dimensionless variables are defined as

$$u^* = \frac{u}{\bar{u}_0}, \quad v^* = \frac{v}{\bar{u}_0}, \quad z^* = \frac{z}{R_0}, \quad r^* = \frac{r}{R_0}, \quad p^* = \frac{p}{\rho{\bar{u}_0}^2} \tag{83}$$

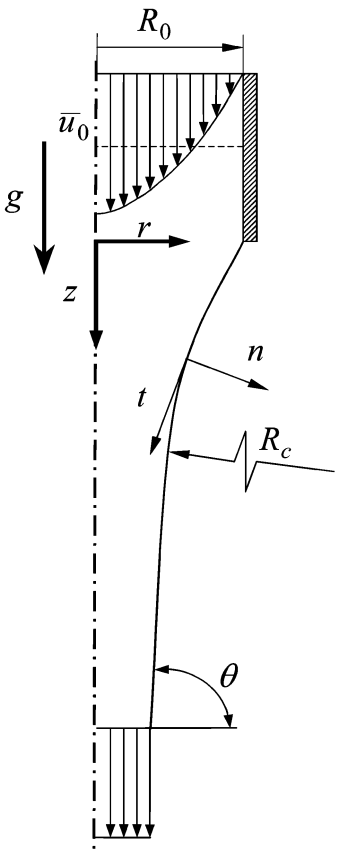

Figure 4. Model of the axisymmetric jet flow: R_0, nozzle radius; $\bar{u}_0$, mean nozzle exit velocity; g, gravitational acceleration; R_c, curvature parameter; θ, downstream contact angle; (r, z), cylindrical polar coordinate system; (n, t), local normal tangential coordinate system.

where the mean nozzle exit velocity, $\bar{u}_0$, and the nozzle radius, R_0, serve as the characteristic jet flow parameters. Two dimensionless numbers are derived: the Reynolds number, *Re*, which was defined in eq 16, and the Froude number, *Fr*, which is given by eq 78.

3.2. Computational Domain and Meshing. A short part of the long capillary nozzle is considered in Figure 4. We must allow for a sufficient distance between the inlet of the jet flow domain and the nozzle exit plane so that the inlet boundary conditions can be applied safely. The nozzle section was chosen to be one nozzle radius in length, which was found to be sufficient for the flow parameters under consideration in this study. The jet model ends at a downstream position sufficiently far away from the nozzle that the appropriate downstream boundary conditions may be applied. To keep the numerical size of the flow to a minimum, we chose a length of $100R_0$ for the free jet section.

The surrounding air is neglected in the model and treated as a vacuum; the pressure of the adjacent phase is set equal to zero and the only pressure exerted on the free surface of the jet is through the action of surface tension. Because the jet surface is curved, the pressure at the surface of the jet cannot be uniform.

Figure 5 shows the mesh that was used in the numerical computations presented in this paper. The section of the mesh displayed in Figure 5 spans $\Delta z = 8.2$ μm in the axial direction and $\Delta r = 5.5$ μm in the radial direction around the nozzle exit at $r = R_0$ and $z = 0$ for a nozzle radius of $R_0 = 0.79$ mm. The grid was generated using FLUENT's mesh-generating program

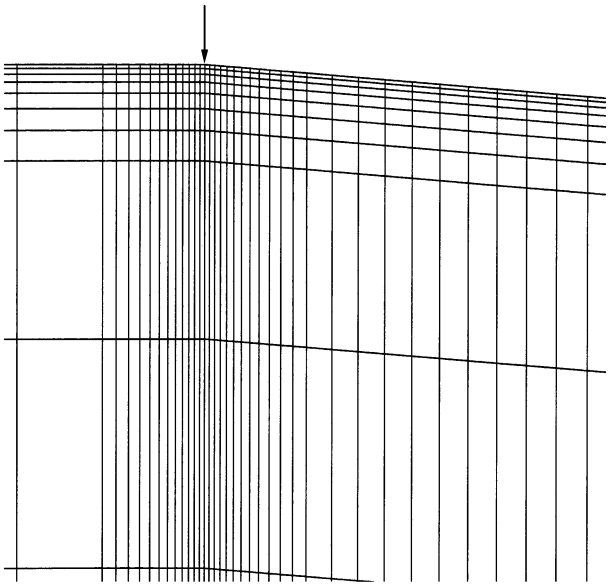

Figure 5. Regular mesh of the jet flow around the nozzle exit region after deformation. The section spans $\Delta z = 8.2$ μm in the axial direction and $\Delta r = 5.5$ μm in the radial direction around the nozzle exit at $r = R_0 = 0.79$ mm and $z = 0$ (marked by the arrow).

GAMBIT. The relatively simple axisymmetric flow geometry permits the use of a regular mesh. At the detachment point, where the free surface starts to develop, the boundary condition changes from a no-slip condition at the wall to a slip condition on the free surface, which results in a rapid velocity increase at this point. Dense meshing is required around the point of detachment to capture the steep velocity gradients in the axial flow direction accurately.

In the radial direction, the hydrodynamic and diffusion boundary layers, ϵ and ϵ_c, start to grow at the point of detachment. The two boundary layers are related through

$$\frac{\epsilon_c}{\epsilon} \sim \sqrt{\frac{\rho D}{\mu}} = \frac{1}{\sqrt{Sc}} \tag{84}$$

For an aqueous surfactant solution of C_{16}TAB, we find that $\epsilon_c/\epsilon \sim \mathcal{O}(10^{-2})$. The thickness of the diffusion boundary layer is given by

$$\epsilon_c \sim \sqrt{\frac{D}{\mathrm{d}u_s/\mathrm{d}z}} \tag{85}$$

For C_{16}TAB (see Table 2), we can estimate ϵ_c to be $\mathcal{O}$(1 μm). Figure 5 shows that the mesh immediately underneath the surface is very dense to account for the smallness of the diffusion boundary layer. The distance from the row of surface nodes to the first row of nodes underneath the surface is only about 40 nm (for a nozzle radius of $R_0 = 0.79$ mm), to ensure the accurate computation of the concentration field within the diffusion boundary layer. The mesh consists of 12 012 elements in total, which resulted in average computation times of not more than 10 min for the water jet and not more than 30 min if the hydrodynamics were solved along with the coupled mass-transfer problem on a Windows 2000 PC with 512 MB RAM and a 1.0 GHz processor. A fully coupled Newton−Raphson iteration scheme, where the free surface position was updated at each iteration step, was employed to solve the

governing set of equations. The free surface position was adjusted by moving the nodes on the surface and underneath the surface along the so-called spines to satisfy the kinematic condition, eq 94.

3.3. Boundary Conditions. 3.3.1. Inlet. Fully developed laminar flow is applied at the inlet of the flow domain

$$u^*(r^*,z^*\ll 0) = 2(1 - r^{*2}) \quad \text{and} \quad v^*(z^*\ll 0) = 0 \tag{86}$$

3.3.2. Nozzle Wall. A no-slip condition is applied at the nozzle wall

$$u^*(r^*=1.0,z^*\leqslant 0) = 0 \quad \text{and} \quad v^*(r^*=1.0,z^*\leqslant 0) = 0 \tag{87}$$

3.3.3. Center Line. Symmetry conditions are found on the axial center line of the jet

$$\frac{\partial u^*}{\partial r^*}(r^*=0,z^*) = 0 \quad \text{and} \quad v^*(r^*=0,z^*) = 0 \tag{88}$$

3.3.4. Outlet. In the absence of gravity, a radially uniform axial velocity distribution and a final jet diameter are approached asymptotically as the distance from the jet nozzle is increased, that is, $\theta \rightarrow \pi/2$ and $v^* \rightarrow 0$ for $z^* \gg 0$, where θ is the contact angle at the outlet of the jet flow domain (see Figure 4). In the presence of gravity, the jet continues to contract and does not reach a final diameter. We presume that, for a long enough jet, the inertia term will eventually grow so that it overwhelms viscous forces and balances the gravitational term, thus leading to a free-fall velocity field.[19] This condition requires that $\theta < \pi/2$. Applying Bernoulli's law and the equation of continuity and accounting for the parabolic velocity profile at the nozzle exit yields a value for the contact angle, θ, that is applied at the outlet of the jet flow domain. Thus,

$$\theta(z^*\gg 0,r^*=R^*) = \frac{\pi}{2} - \arctan\left[-\frac{1}{4Fr}\left(\frac{4}{3} + \frac{z^*}{Fr}\right)^{-5/4}\right] \tag{89}$$

where $R^* = R/R_0$ is the dimensionless radial position of the free surface. Continuous contraction of the jet results in a velocity profile that is not exactly uniform in the radial direction. The symmetry condition requires $v^*(r^*=0) = 0$, but v^* increases with increasing r^*, reaching its maximum value at the surface ($r^* = R^*$). This maximum value may be expressed in terms of the contact angle, θ, and the axial jet velocity component, u^*, as

$$v^*(z^*\gg 0,r^*=R^*) = u^* \tan\left(\frac{\pi}{2} - \theta\right) \approx u^*\left(\frac{\pi}{2} - \theta\right) \tag{90}$$

The smallness of $\pi/2 - \theta$, which is of order 10^{-4}, leads to very small values for $v^*(z^*\gg 0,r^*=R^*)$. However, downstream boundary conditions formulated by requiring that all velocity gradients vanish result in an inconsistent flow field for a vertical jet. Therefore, only the contact angle, $\theta(z^*\gg 0,r^*=R^*)$, defined in eq 89, is applied as a downstream boundary condition.

The curvature in the azimuthal direction and the nonzero surface tension value dictate that the pressure at the common node between the free surface and the outlet is nonzero. If there is no boundary condition specified on the normal component of velocity at the outlet, which is the case, the so-called stress-free natural boundary condition is applied in FIDAP, which is

$$-p + 2\mu \frac{\partial u_n}{\partial n} = 0 \tag{91}$$

where p is the pressure, μ is the viscosity, u_n is the normal component of velocity, and n is the normal to the outlet. Note that in the jet flow geometry the direction of the normal at the outlet of the flow domain is identical with the axial direction of flow. If the flow is fully developed (or nearly fully developed) at the outlet (making the derivative $\partial u_n/\partial n$ zero, or nearly zero) or if the viscous contribution is small, then eq 91 effectively makes the pressure zero at the outlet, which conflicts with the nonzero pressure at the outlet node caused by the curvature and the nonzero surface tension value. Removing the pressure term from eq 91 resolves this conflict.

3.3.5. Free Surface. A normal stress condition on the jet surface (the ambient pressure is set equal to zero) accounts for the varying pressure along the jet axis due to the curvature of the jet surface. Using the Young−Laplace equation, we obtain

$$\frac{Re}{2}\tau_n^* = 2R_c^*\frac{1}{Ca} \tag{92}$$

where $R_c^* = R_c R_0$ is the dimensionless curvature parameter, which is defined in the usual way (see, for example, the work of Middleman[13]), and Ca is the Capillary number. The dimensionless normal stress component is defined as $\tau_n^* = \tau_n(\rho\bar{u}_0^2)^{-1}$.

The dimensionless tangential stress component, $\tau_t^* = \tau_t(\rho\bar{u}_0^2)^{-1}$, is only active in the case of varying surface tension along the jet length and is zero for a pure liquid. The tangential stress boundary condition couples the jet hydrodynamics and the mass transfer and is responsible for the occurrence of the Marangoni effect. It reads

$$\frac{Re}{2}\tau_t^* = \frac{\partial}{\partial t^*}\frac{1}{Ca} = \frac{\partial u_t^*}{\partial n^*} \tag{93}$$

In eq 93, $t^* = t/R_0$ and $n^* = n/R_0$ define the dimensionless local tangential and normal coordinate system on the free surface, and $u_t^* = u_t/\bar{u}_0$ is the tangential surface velocity component.

A kinematic condition that sets the normal velocity, $u_n^* = u_n/\bar{u}_0$, on the free surface to zero is used to locate the position of the free surface

$$u_n^* = 0 \tag{94}$$

3.4. Surface Velocity and Contraction in the Water Jet. The computed surface velocity, u_s^*, and the free surface position, R^*, of the water jet (that is, without surfactant) are plotted in Figure 6 as a function of the axial jet coordinate, z^*, for $Re = 1950$. Also plotted in Figure 6 is the theoretical solution found by Goren, eqs 18 and 19, and the theoretical solution that is derived in this work, eqs 15 and 17. We have given a comparison of our numerical and experimental results in part 1 of this series of papers, which shows excellent agreement.[6]

At larger values of z^*, our boundary-layer theory underpredicts the surface velocity and the contraction in the jet flow, whereas Goren's theory overpredicts both variables. At small z^*, both theories overpredict the surface velocity and jet contraction. We note here that the analytical theory has relative errors $\mathcal{O}(Re^{-1/3})$, as

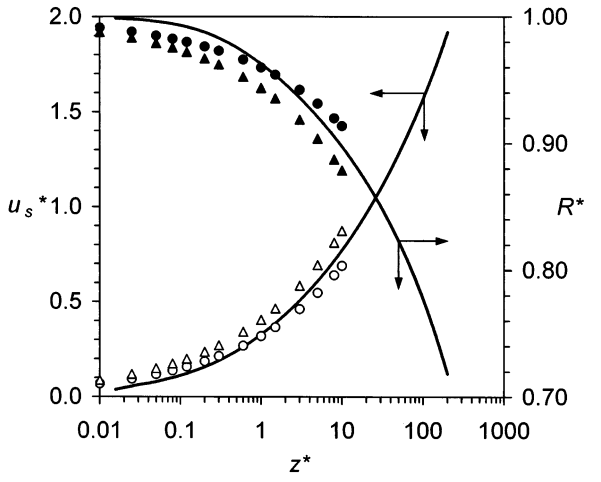

Figure 6. Surface velocity, $u_s^* = u_s/\bar{u}_0$, and surface position, $R^* = R/R_0$, of the water jet as a function of the jet length, $z^* = z/R_0$. The data are for $Re = 1950$, $Ca^{-1} = Ca_w^{-1} = 58.9$, and $(2Fr)^{-1} = 0.005\,07$. The lines are the numerical solution. The open and closed circles are given by eqs 15 and 17, respectively. Goren's theoretical results, eqs 18 and 19, are the open and closed triangles, respectively.

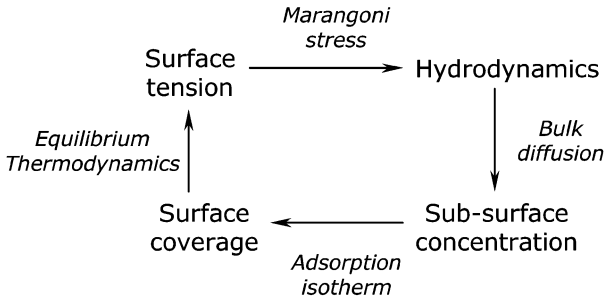

Figure 7. Model of diffusion-controlled surfactant adsorption in the jet flow.

demonstrated by Tillett.[12] This gives a relative error of about 0.08 for a Reynolds number of nearly 2000, which is consistent with the differences noted in Figure 6. Although not shown here, the same difference between the numerical solution and the analytical values was noted at lower Reynolds numbers of 1550 and 1280.

The very rapid acceleration of fluid particles in the surface close to the point of emergence from the nozzle is evident. This acceleration results in very high surface expansion rates, du_s^*/dz^*, near the nozzle exit, which provide the driving force for the diffusion of the surfactant molecules to the surface, as will be discussed in the following section.

4. Surfactant Adsorption in the Jet Flow

The adsorption of surfactant monomers at the jet surface may be divided into a four-step mechanism, which is depicted in Figure 7. Our adsorption model is based on these steps. First, surfactant monomers are transported to the surface of the jet through diffusion and convection from the bulk (i). In the case of the jet, diffusion is the main mechanism that is responsible for the delivery of surfactant molecules to the surface. This diffusive flux toward the jet surface is balanced by convection within the surface, which is determined by the rate of surface expansion. On the assumption of local equilibrium at the surface, the subsurface concentration and surface coverage may be related by an appropriate adsorption isotherm (ii). Surface coverage and surface tension are linked by a thermodynamical equilibrium expression, the Szyszkowski equation (see below, eq 103), where the small contribution of the diffusion layer to the dynamic surface tension has been neglected (iii). Finally, the tangential surface stress boundary condition (93) couples mass transfer and fluid mechanics of the jet and leads to the occurrence of the Marangoni effect (iv).

The same physical assumptions were made in the surfactant mass-transfer model of the overflowing cylinder (OFC),[21,20] which was previously modeled numerically by Schunk,[22] who also predicted surfactant adsorption in slide coating using this model.[23] Recently, Ghadiali et al.[24] presented a numerical model of surfactant adsorption at the interface of a semi-infinite bubble progressing in a capillary tube, which matches the model outlined in Figure 7. Cerro and Whitaker used the model in their theoretical study on the hydrodynamic development of thin films in the presence of surfactant.[25]

4.1. Bulk Diffusion and Convection of Surfactant. The convection−diffusion equation describes the transport of surfactant molecules from the core of the jet toward the free surface. In cylindrical polar coordinates (r^*, z^*), this conservation equation for a surfactant species being transported in the fluid under steady-state flow conditions is given in its dimensionless form as

$$\frac{Re}{2}Sc\left(v^*\frac{\partial w}{\partial r^*} + u^*\frac{\partial w}{\partial z^*}\right) = \left[\frac{1}{r^*}\frac{\partial}{\partial r^*}\left(r^*\frac{\partial w}{\partial r^*}\right) + \frac{\partial^2 w}{\partial z^{*2}}\right] \quad (95)$$

Equation 95 is given in terms of the mass fraction of surfactant species, w. The Schmidt number, Sc, is defined in eq 42.

4.2. Boundary Conditions. 4.2.1. Inlet. At the inlet of the jet flow domain, sufficiently far upstream from the nozzle exit plane, the bulk concentration, w_b, is assumed everywhere in the fluid, that is

$$w(r^*, z^* \ll 0) = w_b \quad (96)$$

4.2.2. Nozzle Wall. The nozzle wall is made impenetrable for surfactant, and thus

$$\frac{1}{r^*}\frac{\partial}{\partial r^*}(r^* w) = 0 \qquad \text{at } r^* = 1.0,\ z^* \leqslant 0 \quad (97)$$

4.2.3. Free Surface. A flux boundary condition at the free surface of the jet allows the surface to take up surfactant from the bulk liquid. Hence, a diffusive mass flux that is directed along the outward unit normal of the free surface is prescribed on that boundary. This diffusive mass flux is given as

$$q^*_{s,diff} = -\left(\frac{1}{r^*}\frac{\partial}{\partial r^*}(r^* w_s) + \frac{\partial w_s}{\partial z^*}\right) \qquad \text{at } r^* = R^*,\ z^* > 0 \quad (98)$$

where w_s refers to the subsurface concentration. In eq 98, the dimensionless diffusive mass flux is defined as $q^*_{s,diff} = (\rho D/R_0)^{-1} q_{s,diff}$. This diffusive mass flux, $q^*_{s,diff}$, of surfactant molecules is balanced by the rate of local redistribution by surface convection, $q^*_{s,conv} = (\rho D/R_0)^{-1} q_{s,conv}$, which can be written as

$$q^*_{s,conv} \approx \frac{M\Gamma_{sat}\bar{u}_0}{\rho D}\frac{d}{dz^*}(\Gamma^* u_s^*) \qquad \text{at } r^* = R^*,\ z^* > 0 \quad (99)$$

In the high Reynolds number limit, the contraction of the jet is slight, which allowed us to simplify eq 99. It is sufficient to consider the axial component of the tangential surface velocity, $u_t^* \approx u_s^*(z^*)$, and we can then replace the surface gradient with the gradient in the axial direction, d/dz^*.

The surface coverage, Γ^*, in eq 99 must be linked to the subsurface concentration, w_s, to enable matching of diffusive and convective flux. Here, we assume diffusion-controlled surfactant adsorption; that is, each molecule that is being transported to the surface adsorbs immediately, and diffusion is the rate-controlling transport step. On the basis of this assumption of local equilibrium everywhere along the jet surface, an equilibrium adsorption isotherm is used to link Γ^* and w_s. The simplest nonlinear isotherm is the Langmuir isotherm,[26] given as

$$\Gamma^* = \frac{\Gamma}{\Gamma_{sat}} = \frac{w_s}{k^* + w_s} \tag{100}$$

where $k^* = Mk/\rho$ is the dimensionless Langmuir constant. Replacing Γ^* with eq 100 in eq 99 leads to the expression for the convective mass flux that is applied at the free surface of the jet. It reads

$$q^*_{s,conv} = \frac{M\Gamma_{sat}\bar{u}_0}{D\rho}(k^* + w_s)^{-1}\left[u_s^* \frac{dw_s}{dz^*}\left(\frac{k^*}{k^* + w_s}\right) + w_s \frac{du_s^*}{dz^*}\right] \tag{101}$$

Equation 101 provides the driving force for the transport of surfactant molecules (almost exclusively by diffusion) to the surface or, to be more precise, to the subsurface. It is implemented into the CFD code FIDAP through a Fortran user subroutine. The derivatives, du_s^*/dz^* and dw_s/dz^*, within the user subroutine are computed using fourth-order finite-difference approximations. Here, we have employed an algorithm published by Fornberg to compute the weights of the finite-difference approximations on arbitrarily spaced grids.[27]

In the CFD code FIDAP, by default, an applied flux that results in a net flow into the fluid would be specified as positive. When programming eq 101 into the CFD code, we have therefore introduced a negative sign in the equation to account for the fact that the surfactant molecules diffuse toward the surface.

4.2.4. Outlet. In the absence of gravity, significantly far downstream from the nozzle exit plane, equilibrium conditions are reached at the surface, that is, $w_s(z \gg 0) \rightarrow w_b$. In the presence of gravity, however, the surface experiences constant expansion at the downstream position, and equilibrium conditions are never reached. Consequently, no constraints to the subsurface concentration are applied at the outlet of the jet flow domain.

4.3. Coupling of Hydrodynamics and Surfactant Adsorption: Marangoni Flow in the Jet. The link between the surface tension and surface coverage is established by means of the Frumkin equation

$$\sigma = \sigma_w + N\mathcal{R}T\Gamma_{sat} \ln\left(1 - \frac{\Gamma}{\Gamma_{sat}}\right) \tag{102}$$

which, in terms of the subsurface concentration and using our dimensionless notation, may be given as

$$\frac{1}{Ca} = \frac{1}{Ca_w} + E \ln\left(1 - \frac{w_s}{k^* + w_s}\right) \tag{103}$$

Equation 103 is known as the Szyszkowski equation,[28] in which $1/Ca_w = \sigma_w(\mu\bar{u}_0)^{-1}$ is the surface tension parameter of pure water. Equation 103 is implemented into the CFD code FIDAP through a Fortran user subroutine. The Elasticity number, E, is defined in eq 52.

The tangential stress boundary condition, eq 93, becomes active when the surface tension parameter, $1/Ca$, is not constant but varies along the jet length z^*.

4.4. Limiting Marangoni Stress at the Point of Detachment: Hybrid CFD Model. Converged numerical solutions of the CFD model as outlined above are only achieved at very low values for the bulk concentration c_b of about 0.01 mol m^{-3} at $Re = 1950$. At higher bulk concentrations, direct coupling of surfactant adsorption and fluid mechanics—the link between the shear stress condition (eq 93) and the equation of state (eq 103)—led to failure of the Newton–Raphson iteration scheme. The Marangoni stress, d/dz^* $(1/Ca)$, very near to $z^* = 0$ was found to exceed the shear stress at the nozzle wall, as a consequence of which the surface velocity was not only reduced but also brought to rest and reversed. The result was the appearance of a closed vortex flow, much less in diameter than the nozzle radius, in the nozzle exit plane. With the occurrence of such a toroidal flow, convergence for the convection–diffusion equation could no longer be attained. Schunk[22] reported a similar phenomenon in his numerical work on surfactant adsorption in an OFC, where what he believed to be an oscillatory toroidal instability, which was caused by steep surface tension gradients, was observed near the center of the OFC.

The failure of our numerical scheme results from its inability to handle the step change in the subsurface concentration that should occur at the point of detachment. To speed up convergence and to suppress the appearance of oscillations in the numerical solutions, we have introduced upwinding,[29] a degree of numerical diffusion that does not affect the solution away from the nozzle. The CFD code FIDAP uses a streamline upwinding scheme that adds numerical diffusion only along the flow direction.[30] Axial diffusion and upwinding cause the step change in the surface concentration to be smeared out over a few nodes, resulting in finite, but very large, concentration gradients immediately downstream of the point of detachment. When these concentration gradients are converted to surface tension gradients through the equation of state, large accelerations result. The whole calculation scheme then fails to converge.

We have tackled this problem by combining the theoretical solution at the nozzle exit with the far-field solution that is obtained from the numerical computation. We apply a limiting Marangoni stress at the point of detachment. We also apply the finite surface concentration, Γ_0^*, at $z^* = 0$, which has been calculated from the theory. Stable solutions for the convection–diffusion equation are then obtained for a range of bulk concentrations at our high Reynolds numbers. The implementation in our numerical model is detailed in the next sections.

We note here that our boundary-layer theory is based on the supposition that reverse flow does not occur and consequently that the maximum Marangoni stress does

not exceed the stress value at the nozzle wall. We have shown that this assumption can lead to a solution that does not show singular behavior at the point of detachment. Our analysis, however, does not exclude the possibility that other families of solutions exist, such as the toroidal vortices observed in some of the numerical solutions.

4.4.1. Limitation Condition and Concentration Profile in the Region of Detachment. The condition that determines the Marangoni stress at the point of detachment is given by eq 54. This limitation is implemented into the numerical computation through the subsurface concentration profile, $w_s(z^*)$, at the point of detachment at $z^* = 0$. The surface equation of state (103) determines the surface tension everywhere along the jet surface, including the point of detachment at $z^* = 0$. It must thus fulfill the limitation condition (54). Differentiating the Szyszkowski equation (54) with respect to z^*, and considering the limitation condition, gives

$$\frac{\mathrm{d}}{\mathrm{d}z^*}\left(\frac{1}{Ca}\right) = -\frac{E}{k^* + w_s}\frac{\mathrm{d}w_s}{\mathrm{d}z^*} = -4 \qquad (104)$$

at $z^* = 0$. Integrating eq 104 by separating the variables gives

$$\frac{k^* + w_s}{k^* + w_{s,0}} = \exp\left(\frac{4}{E}z^*\right) \qquad (105)$$

In eq 105, $w_{s,0}$ is the subsurface concentration at the point of detachment ($z^* = 0$), for which we have to make a suitable choice. For small values of z^*, eq 105 can be linearized and rearranged to give the solution for w_s, which is valid as $z^* \to 0$, namely

$$w_s = w_{s,0} + \frac{4}{E}(k^* + w_{s,0})z^* \qquad (106)$$

4.4.2. Asymptotic Matching with the Numerical Far-Field Solution. We match the linear solution for $w_s(z^*)$ at the point of detachment, eq 106, with the numerical downstream solution for w_s that is computed by the CFD code. To carry out the matching, we approximate the numerical downstream solution with a power-law equation of the form

$$w_s = \mathcal{C} z^{*m} \qquad (107)$$

with $\mathcal{C}$ and m being the parameters of the least-squares power-law fit.

Asymptotic matching of eqs 106 and 107 leads to a smooth solution for w_s that holds everywhere along the jet surface. We have used

$$w_s = \left[w_{s,0} + \frac{4}{E}(k^* + w_{s,0})z^*\right]\left[\frac{l^{*2}}{l^{*2} + z^{*2}}\right]^{1(-m)/2} \qquad (108)$$

with

$$l^* = \frac{l}{R_0} = \left\{\frac{\mathcal{C}}{\frac{4}{E}(k^* + w_{s,0})}\right\}^{1/(1-m)} \qquad (109)$$

Equation 108 provides us with a smooth fit through the downstream solution for w_s that is computed by the CFD code and gives the required maximum Marangoni stress at the point of detachment. This information is passed to the numerical computation through the equation of state (103), which is linked to eq 108 instead of coupling it directly with the numerical solution for the subsurface concentration. In this way, a smooth surface tension function, $Ca^{-1}(z^*)$, is obtained that accounts for the limiting Marangoni stress at the point of detachment. The parameters of the power-law fit in eq 107, $\mathcal{C}$ and m, are updated to fit the numerical downstream solution after each computation, until a stable solution is obtained. Typically, five or six computations were necessary to attain stable solutions. Note that "downstream solution" here refers to the region of the jet flow where $z^* \gg l^*$.

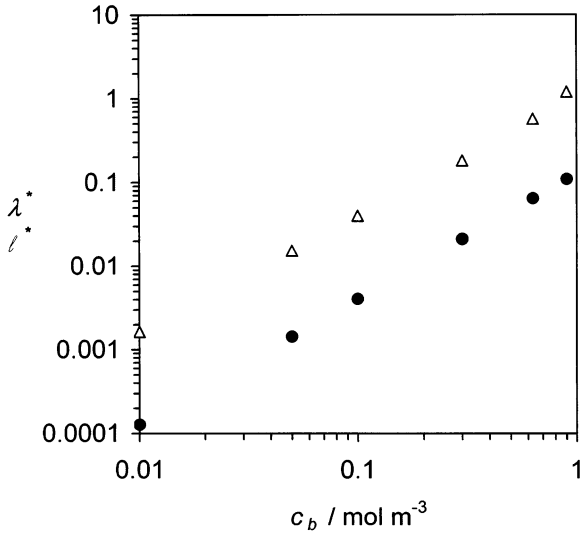

Figure 8. Length of the detachment region, $\lambda^* = \lambda/R_0$ (closed circles, eq 73), and the related parameter, $l^* = l/R_0$ (open triangles, eq 109), as a function of the bulk concentration, c_b, of C_{16}TAB at $Re = 1950$ and $(2Fr)^{-1} = 0.00507$.

In eq 108, l^* is a dimensionless length scale that is related to the length of the detachment region, λ^*, because it marks the point of transition from the (linear) upstream solution (eq 106) to the downstream solution (eq 107). The length scale l^* is a function of the power-law parameters $\mathcal{C}$ and m, which, in turn, depend on the bulk concentration c_b, the Reynolds number, and the physicochemical properties of the surfactant. The values for $\mathcal{C}$ and m are displayed in Table 1 for $Re = 1950$ and the properties of C_{16}TAB (given in Table 2) and different bulk concentrations c_b.

Equation 74 provides an estimate of the finite value of the surface concentration at the point of detachment, $\Gamma_0^* = \Gamma^*(z^*=0)$. Using the Langmuir isotherm, eq 100, we can calculate a value for the subsurface concentration at that point, $w_{s,0} = w_s(z^*=0)$, which is then used in eqs 108 and 109. The values for Γ_0^* and $w_{s,0}$ that we calculated using the physical properties of an aqueous solution of C_{16}TAB are summarized in Table 1 for the bulk concentrations under consideration in this work.

Figure 8 shows how λ^* and l^* depend on the bulk concentration, c_b, for a Reynolds number of $Re = 1950$ and the surfactant properties of C_{16}TAB. Both sets of values increase monotonically with increasing bulk concentration and, in the limit of $c_b \to 0$, correctly show λ^*, $l^* \to 0$. The λ^* values have a $^3/_2$ power dependence on c_b (see eq 73), and the l^* values show the same functional dependence on c_b.

Although the length scale l^* is related to λ^*, which explains the same functional dependence on c_b, the

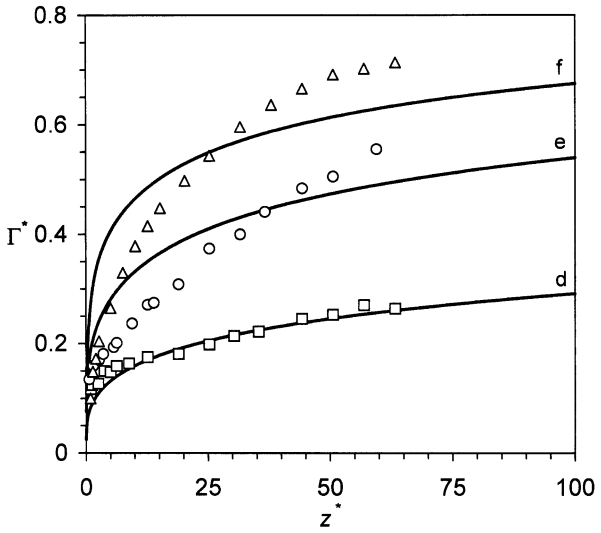

Figure 9. Surface coverage, $\Gamma^* = \Gamma/\Gamma_{sat}$, as a function of the axial jet coordinate, $z^* = z/R_0$, at $Re = 1950$ and $(2Fr)^{-1} = 0.00507$. Bulk concentrations of $c_b = 0.3$ mol m^{-3} (d), 0.63 mol m^{-3} (e), and 0.9 mol m^{-3} (f) C_{16}TAB in water are shown. The symbols are the experimental data at $c_b = 0.3$ mol m^{-3} (squares), 0.63 mol m^{-3} (circles), and 0.9 mol m^{-3} (triangles).

values for l^* are about one order of magnitude larger than the values for λ^*. This difference in magnitude has its origin in the way both are defined. We remember that λ^* is defined as the point where the detachment region velocity solution is matched with a far-field solution that is extrapolated back to this point. In contrast, l^* indicates the distance at which a linear dependence of the subsurface concentration near to the nozzle makes a transition to the fitted power-law dependence of the computed solution for large z^*.

4.5. Surface Concentration in the Liquid Jet. Figures 9 and 10 show computed surface coverage profiles. The surfactant chosen is C_{16}TAB, which has a cmc of 0.92 mol m^{-3}. The values of the physical parameters that have been used in the computations are displayed in Table 2. The bulk concentrations are all below the cmc, and the Reynolds number is high, at $Re = 1950$.

In Figure 9, experimentally obtained surface coverage data for $c_b = 0.3$, 0.63, and 0.9 mol m^{-3} are compared with the computed values from our model. The experimental surface coverage data were obtained from ellipticity measurements in the jet flow, details of which can be found in part 1 of this series of papers.[6] We can see very clearly that the jet surface is depleted of surfactant near the nozzle exit because of the rapid surface expansion in this region of the jet. The surface coverage increases quite rapidly in the close vicinity of the nozzle exit. The increase of Γ^* with increasing z^* is less pronounced in the downstream region of the jet because of a decrease in the surface expansion. At $c_b = 0.3$ mol m^{-3}, the predicted values and the measured data exhibit a very good agreement. At $c_b = 0.63$ and 0.9 mol m^{-3}, the agreement is less good. At these higher concentrations, very near the cmc, the experimental data show that $\Gamma^*(z^*)$ increases less rapidly as the jet leaves the nozzle than the computed results suggest. Furthermore, at these high concentrations, the experimental data approach the state of equilibrium at the surface sooner than the computed values.

Although the estimates for Γ_0^* that were used in the numerical computations agree reasonably well with the first experimental values for Γ^* at small z^*, the diffusion-controlled modeling approach with a Langmuir-type isotherm of the CFD model seems to fail to correctly predict the adsorption behavior of C_{16}TAB in the jet at bulk concentrations around the cmc. Our model neglects the presence of an electric double layer, which has the effect of reducing the rate of mass transfer to the surface, because adsorbing molecules must overcome the electrostatic resistance of the surface.[31] This model deficiency might explain the deviation between the computation and the experimentally obtained values at higher bulk concentrations.

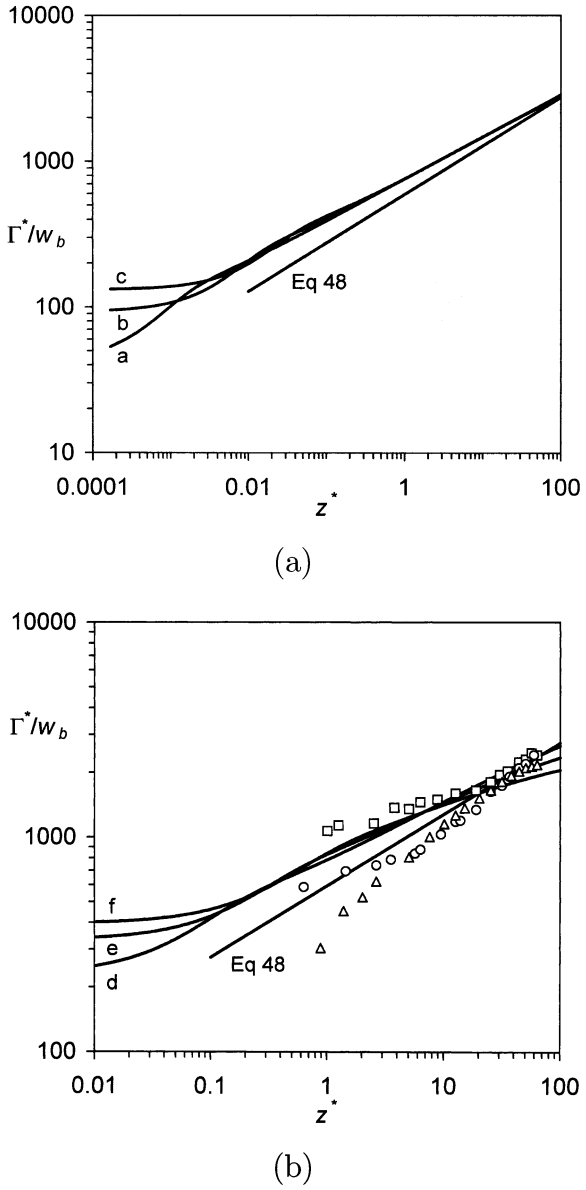

Figure 10. (a and b) Γ^*/w_b as a function of z^*, at $Re = 1950$ and $(2Fr)^{-1} = 0.005\,07$. Bulk concentrations of $c_b = 0.01$ mol m^{-3} (a), 0.05 mol m^{-3} (b), 0.1 mol m^{-3} (c), 0.3 mol m^{-3} (d, squares), 0.63 mol m^{-3} (e, circles), and 0.9 mol m^{-3} (f, triangles) C_{16}TAB in water are shown. Equation 48, which states that $\Gamma^*/w_b \sim z^{*1/3}$, is also plotted.

Equation 48 suggests that, in the far field, $\Gamma^*/w_b \sim z^{*1/3}$. Parts a and b of Figure 10 show that the experimental data do indeed converge when Γ^*/w_b is plotted as a function of z^*, at larger z^*. Equation 48 is also plotted in Figure 10a,b, together with the computed hybrid solution. The undulations in some of the computed solutions are probably numerical artifacts.

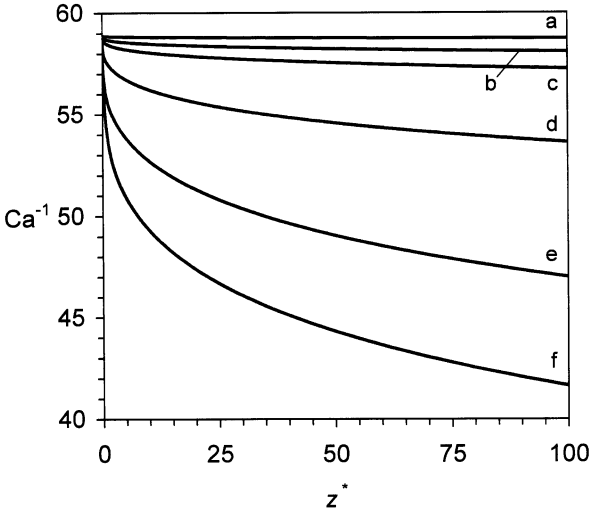

Figure 11. Surface tension parameter, $Ca^{-1} = \sigma(\mu\bar{u}_0)^{-1}$, as a function of the axial jet coordinate, $z^* = z/R_0$, at $Re = 1950$ and $(2Fr)^{-1} = 0.005\,07$. Bulk concentrations of $c_b = 0.01$ mol m^{-3} (a), 0.05 mol m^{-3} (b), 0.1 mol m^{-3} (c), 0.3 mol m^{-3} (d), 0.63 mol m^{-3} (e), and 0.9 mol m^{-3} (f) C_{16}TAB in water.

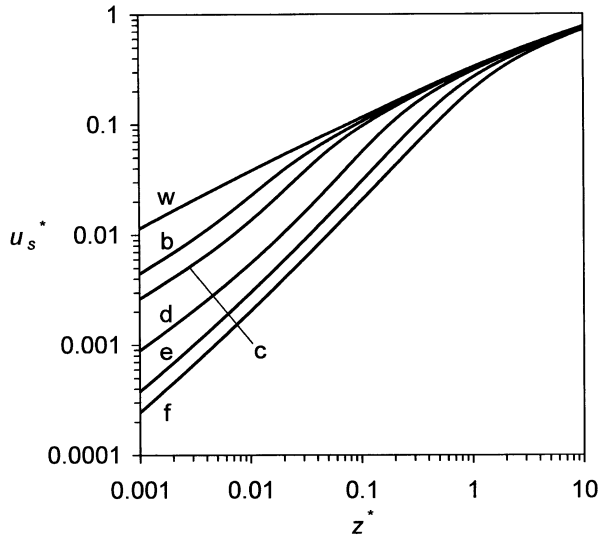

Figure 12. Surface velocity profiles, $u_s^* = u_s^*(z^*)$, for the bulk concentrations $c_b = 0.05$ mol m^{-3} (b), 0.1 mol m^{-3} (c), 0.3 mol m^{-3} (d), 0.63 mol m^{-3} (e), and 0.9 mol m^{-3} (f) C_{16}TAB in water at $Re = 1950$ and $(2Fr)^{-1} = 0.005\,07$ in comparison with the $u_s^*(z^*)$ profile of the water jet (w).

4.6. Dynamic Surface Tension in the Liquid Jet. The dynamic surface tension calculations, $Ca^{-1} = Ca^{-1}(z^*)$, that correspond to the computed surface coverage data shown in Figures 9 and 10 are shown in Figure 11. At the lowest concentration, $c_b = 0.01$ mol m^{-3}, the surface tension parameter remains nearly that of water and changes only very slightly over the length of the jet, which agrees with the low surface coverage values at this concentration (see Figure 10a). We also note that only very small quantities of surfactant adsorb at the point of detachment at low bulk concentrations (curves a−c in Figure 11) and the surface tension parameter at that point is nearly that of pure water; that is, $Ca^{-1}(z^*=0) \approx Ca_w^{-1} = 58.9$. At the point of detachment, from eq 54, the local surface tension gradient is identical for all bulk concentrations; that is, $\mathrm{d}/\mathrm{d}z^*\ (Ca^{-1}) = -4$ at $z^* = 0$. Within the region of detachment, the local Marangoni stress is linear, eq 56. Outside the region of detachment, $z^* \gg l^*$, higher bulk concentrations lead to steeper surface tension gradients, which persist for significant jet lengths. At the highest concentration (0.9 mol m^{-3}), a relatively rapid decrease in the surface tension is observed, which again is in accordance with the surface coverage data in Figure 9.

4.7. Surface Velocity Profiles in the Liquid Jet. The adsorption of surfactant at the expanding jet surface leads to a surface tension gradient, $\mathrm{d}/\mathrm{d}t^*\ (Ca^{-1}) \approx \mathrm{d}/\mathrm{d}z^*\ (\mathrm{Ca}^{-1})$, that activates the tangential shear stress condition (eq 93). The surface tension gradient acts in the upstream direction (see Figure 11) and retards the jet flow. The theory requires that, in the presence of surfactant, the surface velocity at the point of detachment from the nozzle increases linearly with increasing distance from the nozzle, eq 61. For $z^* \gg l^*$, the Marangoni effect vanishes and the surface velocity tends toward the pure water value. This behavior is shown by the graphs in Figure 12. The linear dependence of u_s^* on z^* for $z^* < l^*$ is clearly visible at higher bulk concentrations. The transition points of all curves compare well with the values for l^* (see Figure 8).

In the experiments, a measurable reduction in the surface velocity was only observed at bulk concentrations well above the cmc. As evident from Figure 12, the surface velocity retardation is rather low and occurs very near the nozzle exit, even at bulk concentrations near the cmc. This position on the jet surface is not fully accessible for the lasers.[6] The theory and calculations presented here are not valid for solutions above the cmc, where micelles are present.

5. Conclusions

In part 2 of this series of papers, we have described a numerical model of surfactant adsorption in a laminar liquid jet, which we have implemented into the CFD code FIDAP. In addition, we have derived an analytical solution of the jet flow in the presence of surfactant, which is based on the limitation of the surfactant-generated Marangoni stress at the point of emergence of liquid from the nozzle. As a consequence of this assumption, the surface velocity, the surface concentration, and the surface tension were found to depend linearly on the axial jet coordinate in the detachment region near the nozzle exit. This contrasts with the solution of the water jet, where the surface velocity shows a cube-root dependence on the axial distance everywhere. The validity of the model that we have presented in this paper is restricted to bulk concentrations well below the cmc and high Reynolds numbers. Furthermore, the model assumes diffusion-controlled adsorption. The predicted surface coverage data agree well with experimental data. The validated adsorption model should be applicable to other free-surface flow configurations, such as coating flows and foaming.

Acknowledgment

We thank EPSRC (GR/M73194) for financial support and Dr. Dimitrina Valkovska for helpful discussions and for providing us with the equilibrium adsorption isotherms of C_{16}TAB. We also thank Professor Howard Stone for helpful comments, and for pointing out the similarity solution to eq 41, and the analogy to the classic Lévêque heat-transfer problem.

Nomenclature

Dimensionless Groups

Ca = Capillary number, $\mu\bar{u}_0/\sigma$
E = Elasticity number, $N\mathscr{R}T\Gamma_{sat}(\mu\bar{u}_0)^{-1}$
Fr = Froude number, $\bar{u}_0^2(2R_0g)^{-1}$
Ma = Marangoni number, $|Ca^{-1} - Ca_0^{-1}|$
Pe = Péclet number, $R_0\bar{u}_0/D$
Re = Reynolds number, $2R_0\rho\bar{u}_0/\mu$
Sc = Schmidt number, $\mu(\rho D)^{-1}$

Latin Symbols

A = dummy parameter, $4\bar{u}_0/R_0$ (s^{-1})
$\mathscr{A}$ = dimensionless constant
a = dummy variable (m s^{-1})
B = dummy parameter, $-2\bar{u}_0/R_0^2$ (m^{-1} s^{-1})
b = dummy parameter (s^{-1})
$\mathscr{C}$ = dimensionless fit parameter
c = molar concentrtaion (mol m^{-3})
D = coefficient of diffusivity (m^2 s^{-1})
$f(z)$ = dependence of u_s on z (m s^{-1})
$f'(z)$ = rate of surface expansion, $du_s(z)/dz$ (s^{-1})
g = gravitational acceleration (9.81 m s^{-2})
k = Langmuir constant (mol m^{-3})
l = length scale (m)
M = molecular weight (kg mol^{-1})
m = power-law parameter
N = ionic number
n = power-law parameter
n = normal surface coordinate (m)
p = pressure (Pa)
q = mass flux (kg m^{-2} s^{-1})
$\mathscr{R}$ = universal gas constant (8.314 J mol^{-1} K^{-1})
R = jet/nozzle radius (m)
R_c = curvature parameter (m^{-1})
r = radial coordinate (m)
T = temperature (K)
t = tangential surface coordinate (m)
U = axial core velocity of the jet (m s^{-1})
$\bar{u}$ = mean jet velocity (m s^{-1})
u = axial jet velocity component (m s^{-1})
v = radial velocity component (m s^{-1})
w = mass fraction, $c(M/\rho)$
y = transverse coordinate in the boundary layer (m)
z = axial coordinate (m)

Greek Symbols

α = surface-slip factor, δ/ϵ
δ = radial distance of the edge of the boundary layer from the nozzle wall (m)
ϵ = thickness of the hydrodynamic boundary layer (m)
ϵ_c = thickness of the diffusion boundary layer (m)
θ = downstream contact angle (deg)
κ = dimensionless constant
λ = length of the detachment region (m)
μ = dynamic viscosity (kg m^{-1} s^{-1})
ν = kinematic viscosity, μ/ρ (m^2 s^{-1})
ρ = density (kg m^{-3})
σ = surface tension (N m^{-1})
τ = stress component (N m^{-2})
Δ = dimensionless downstream surface velocity offset value
$\tilde{\Delta}$ = dimensionless downstream surface concentration offset value
Γ = surface concentration/coverage (mol m^{-2})

Subscripts

0 = point of detachment
b = bulk
conv = convection
diff = diffusion
max = maximum
n = normal direction
s = surface
sat = saturation
t = tangential direction
w = water
wall = nozzle wall
z = downstream position

Superscript

* = dimensionless variable

Literature Cited

(1) Lyklema, J. Fundamentals. *Fundamentals of Interfaces and Colloid Science*; Academic Press: London, 1991; Vol. 1.

(2) Dickinson, E.; Walstra, P. *Food Colloids and Polymers: Stability and Mechanical Properties*; Royal Society of Chemistry: Cambridge, U.K., 1993.

(3) Groteberg, J. B.; Gaver, D. P. A Synopsis of Surfactants Spreading Research. *J. Colloid Interface Sci.* **1996**, *178*, 377−378.

(4) Karsa, D. R. *Industrial Applications of Surfactants 2*; Special Publication No. 77; Royal Society of Chemistry: Cambridge, U.K., 1990.

(5) Lockett, M. J. *Distillation Tray Fundamentals*; Cambridge University Press: Cambridge, U.K., 1986.

(6) Battal, T.; Bain, C. D.; Weiss, M.; Darton, R. C. Surfactant Adsorption and Marangoni Flow in Liquid Jets: I. Experiments. *J. Colloid Interface Sci.* **2003**, *263*, 250−260.

(7) Deen, W. M. *Analysis of Transport Phenomena*; Oxford University Press: Oxford, U.K., 1998.

(8) Scriven, L. E.; Pigford, R. L. Fluid Dynamics and Diffusion Calculations for Laminar Liquid Jets. *AIChE J.* **1959**, *5*, 397−402.

(9) Rideal, E. K.; Sutherland, K. L. The Variation of the Surface Tension of Solutions with Time. *Trans. Faraday Soc.* **1952**, *48*, 1109−1123.

(10) Goren, S. L. Development of the Boundary Layer at a Free Surface from a Uniform Shear Flow. *J. Fluid Mech.* **1966**, *25*, 87−95.

(11) Goren, S. L.; Wronski, S. The Shape of Low-Speed Capillary Jets of Newtonian Liquids. *J. Fluid Mech.* **1966**, *25*, 185−198.

(12) Tillett, J. P. K. On the Laminar Flow in a Free Jet of Liquid at High Reynolds Numbers. *J. Fluid Mech.* **1968**, *32*, 273−292.

(13) Middleman, S. *Modeling Axisymmetric Flows—Dynamics of Films, Jets, and Drops*; Academic Press: San Diego, 1995.

(14) Fisher, R. J.; Denn, M. M.; Tanner, R. I. Initial Profile Development in Melt Spinning. *Ind. Eng. Chem. Fundam.* **1980**, *19*, 195−197.

(15) Dutta, A.; Ryan, M. E. Dynamics of a Creeping Newtonian Jet with Gravity and Surface Tension: A Finite Difference Technique for Solving Steady Free-Surface Flows Using Orthogonal Curvilinear Coordinates. *AIChE J.* **1982**, *28*, 220−232.

(16) Levich, V. G. *Physicochemical Hydrodynamics*; Prentice-Hall: Englewood Cliffs, NJ, 1962.

(17) Georgiou, G. C.; Papanastasiou, T. C.; Wilkes, J. O. Laminar Newtonian Jets at High Reynolds Number and High Surface Tension. *AIChE J.* **1988**, *34*, 1559−1562.

(18) Omodei, B. J. On the Die-Swell of an Axisymmetric Newtonian Jet. *Comput. Fluids* **1980**, *8*, 275−289.

(19) Vrentas, J. S.; Vrentas, C. M.; Shirazi, A. F. Downstream Boundary Conditions for Vertical Jets. *AIChE J.* **1985**, *31*, 1044−1046.

(20) Bain, C. D.; Manning-Benson, S.; Darton, R. C. Rates of Mass Transfer and Adsorption of CTAB at an Expanding Air−Water Interface. *J. Colloid Interface Sci.* **2000**, *229*, 247−256.

(21) Breward, C. J. W.; Darton, R. C.; Howell, P. D.; Ockendon, J. R. The Effect of Surfactants on Expanding Free Surfaces. *Chem. Eng. Sci.* **2001**, *56*, 2867−2878.

(22) Schunk, P. R. Surfactant and Polymer Additives in Coating and Related Flows. Ph.D. Thesis, University of Minnesota, 1989.

(23) Schunk, P. R.; Scriven, L. E. Surfactant Effects in Coating Processes. In *Liquid Film Coating*; Kistler, S. F., Schweizer, P. M., Eds.; Chapman & Hall: London, 1997; Chapter 11d, pp 495−536.

(24) Ghadiali, S. N.; Halpern, D.; Gaver, D. P., III. A Dual-Reciprocity Boundary Element Method for Evaluating Bulk Con-

vective Transport of Surfactant in Free-Surface Flows. *J. Comput. Phys.* **2001**, *171*, 534−559.

(25) Cerro, R. L.; Whitaker, S. The Effect of Surfactants on the Hydrodynamic Development of Thin Liquid Films. *J. Colloid Interface Sci.* **1971**, *37*, 33−51.

(26) Langmuir, I. The Adsorption of Gases on Plane Surfaces of Glass, Mica and Platinum. *J. Am. Chem. Soc.* **1918**, *40*, 1361−1403.

(27) Fornberg, B. Calculation of Weights in Finite Difference Formulas. *SIAM Rev.* **1998**, *40*, 685−691.

(28) von Szyszkowski, B. Experimentelle Studien über kapillare Eigenschaften der wässerigen Lösungen von Fettsäuren. *Z. Phys. Chem.* **1908**, *64*, 385−414.

(29) Anderson, J. D., Jr. *Computational Fluid Dynamics−The Basics with Applications*; McGraw-Hill: New York, 1995.

(30) Hughes, T. J. R.; Brooks, A. N. A Multidimensional Upwind Scheme with no Cross-Wind Diffusion. In *Finite Element Methods for Advection-Dominated Flows*; Hughes, T. J. R., Ed.; ASME Publication ASME-AMD 34; ASME: American Society of Mechanical Engineers: Fairfield, NJ, 1979.

(31) MacLeod, C. A.; Radke, C. J. Charge Effects in the Transient Adsorption of Ionic Surfactants at Fluid Interfaces. *Langmuir* **1994**, *10*, 3555−3566.

Received for review January 17, 2004
Revised manuscript received June 1, 2004
Accepted June 4, 2004

IE049943L